The *JWST* EXCELS survey: Insights into the nature of quenching at cosmic noon

Maya Skarbinski [iD],[1] Kate Rowlands [iD],[2,1] Katherine Alatalo [iD],[3,1] Vivienne Wild [iD],[4] Adam C. Carnall [iD],[5] Omar Almaini [iD],[6] David Maltby,[6] Thomas de Lisle,[6] Timothy Heckman [iD],[1,7] Ryan Begley,[5] Fergus Cullen,[5] James S. Dunlop [iD],[5] Guillaume Hewitt [iD],[6] Ho-Hin Leung [iD],[5] Derek McLeod,[5] Ross McLure,[5] Justin Atsushi Otter [iD],[1] Pallavi Patil,[1] Andreea Petric,[3] Alice E. Shapley,[8] Struan Stevenson,[5] and Elizabeth Taylor [iD][5]

[1] *William H. Miller III Department of Physics and Astronomy, Johns Hopkins University, Baltimore, MD 21218, USA*
[2] *AURA for ESA, Space Telescope Science Institute, 3700 San Martin Drive, Baltimore, MD 21218, USA*
[3] *Space Telescope Science Institute, 3700 San Martin Drive, Baltimore, MD 21218, USA*
[4] *School of Physics and Astronomy, University of St Andrews, North Haugh, St Andrews, KY16 9SS, UK*
[5] *Institute for Astronomy, University of Edinburgh, Royal Observatory, Edinburgh, EH9 3HJ, UK*
[6] *School of Physics and Astronomy, University of Nottingham, University Park, Nottingham NG7 2RD, UK*
[7] *School of Earth and Space Exploration, Arizona State University, Temple, AZ 85287, USA*
[8] *Department of Physics & Astronomy, University of California, 430 Portola Plaza, Los Angeles CA 90095, USA*

ABSTRACT

We study 24 massive quiescent galaxies with $\log M_*/M_\odot > 10$ at $1 < z < 3$ with *JWST*/NIRSpec medium-resolution observations from the Early eXtragalactic Continuum and Emission Line Survey (EXCELS). We reconstruct their star formation histories and find that they have large bursts ($100\ M_\odot \mathrm{yr}^{-1} - 1000\ M_\odot \mathrm{yr}^{-1}$), followed by a rapid truncation of star formation. The number densities of the quenched galaxies in our sample that we predict underwent a submillimeter phase are consistent with submillimeter galaxies being the progenitors of our quenched population. The median post-starburst visibility time is ~ 600 Myr, with more massive galaxies ($\log M_*/M_\odot > 10.7$) exhibiting shorter visibility times than lower mass galaxies. The range of quenching times – defined as the time from the peak starburst to the time of quiescence – found in this sample ($0.06 - 1.75$ Gyr) suggests multiple quenching pathways, consistent with previous studies. We do not see evidence for quenching mechanisms varying with redshift between $1 < z < 3$. We detect evidence for weak AGN activity in 4 out of the 8 galaxies with robust emission line detections, based on line ratio diagnostics. Our findings suggest that there are a diverse range of quenching mechanisms at cosmic noon, and support a scenario in which the primary quenching mechanisms are rapid (< 500 Myr) following a starburst.

1. INTRODUCTION

Constraining the physical mechanisms responsible for the quenching of star formation remains a challenge. Star formation quenching drives the bimodal color distribution in galaxies across cosmic time (e.g. Bell et al. 2004; Arnouts et al. 2007). We begin to see a significant build-up of massive, quenched galaxies during the period referred to as 'cosmic noon' ($1 < z < 3$), when many local passive galaxies are thought to have stopped forming stars (e.g. Fontana et al. 2004; Ilbert et al. 2013; Muzzin et al. 2013; McLeod et al. 2021). However, the bulk of the quenched stellar mass was assembled between $z \sim 1$ and $z \sim 2$, with only a small fraction ($\sim 10\%$) in place

by $z > 2$ (McLeod et al. 2021; Weaver et al. 2023). This raises the question of whether the nature of quenching changes at $z \sim 2$.

Mergers and active galactic nuclei (AGN) feedback are some of the many processes which can contribute to quenching. Mergers may play a crucial role in quenching by suppressing cooling, inducing stellar feedback and/or AGN feedback, and triggering merger-induced shocks (Hopkins et al. 2008a). Gas-rich mergers may induce concentrated bursts of star formation before quenching occurs (e.g. Mihos & Hernquist 1996; Hopkins et al. 2008b; Wellons et al. 2015). Simulations have shown that AGNs may quench galaxies via feedback mecha-

nisms, although direct evidence is lacking and their dependence on redshift is still uncertain (Springel et al. 2005; Khalatyan et al. 2008; Kaviraj et al. 2011). AGN feedback is thought to be the dominant feedback source for massive galaxies ($M_* > 10^{10} M_\odot$) and is expected to be more efficient as the mass of the galaxy increases, thus also increasing the efficiency of quenching (Kaviraj et al. 2007).

Post-starburst galaxies (PSBs) provide an ideal laboratory for studying quenching, as they have undergone a rapid decline in their star formation in the past 1 Gyr. They can be observationally identified by an absence of star-formation-driven nebular emission lines (suggesting low current star formation) coupled with strong Balmer absorption (due to a stellar population dominated by A/F-type stars, indicating that a large fraction of the stellar mass was formed within the last Gyr) (e.g. French 2021). These features result in post-starburst galaxies having distinct spectral energy distribution (SED) shapes, which can be reliably identified using a principal component analysis (PCA) of broadband photometry (Wild et al. 2014), color-color techniques (e.g. Whitaker et al. 2012), and spectroscopic selections (e.g. Wild et al. 2020). PSBs are thought to be an especially important quenching pathway at high redshift, as nearly all quiescent galaxies at $z > 3$ appear to be PSBs (e.g. D'Eugenio et al. 2020; French 2021).

It has been established that galaxies can quench over a range of timescales (e.g. Moutard et al. 2016; Wu et al. 2018; Estrada-Carpenter et al. 2020; Tacchella et al. 2022), suggesting the existence of multiple quenching pathways, with fast quenching potentially becoming increasingly important at higher redshifts (Rowlands et al. 2018; Belli et al. 2019). In order for galaxies to be quenched quickly, the gas supply must have been consumed, heated, or removed through processes such as starbursts, feedback, and/or environmental effects. The typical masses and morphologies of quenching galaxies can vary with redshift (e.g. Wild et al. 2016; Maltby et al. 2018), suggesting that the dominant quenching processes change over cosmic time. At low redshift ($z < 1$), recently and rapidly quenched galaxies tend to have lower stellar masses (Wild et al. 2016), are typically found in dense environments (Wilkinson et al. 2021), and are more disc-dominated (Maltby et al. 2018). In contrast, at $z > 1$, the recently and rapidly quenched population is dominated by massive, compact, spherical galaxies (Wild et al. 2016; Almaini et al. 2017), suggesting internal quenching following a gas-rich compaction event, such as a gas-rich merger. However, the dominant quenching mechanisms at different redshifts are still unresolved.

Prior to *JWST*, we had been limited by small samples of high-resolution, rest-frame optical spectra of post-starburst and quiescent galaxies at higher redshifts ($z > 1$). We now have much larger samples from *JWST* NIRSpec, which has helped constrain the star formation histories (SFHs) of early quiescent galaxies (e.g. Carnall et al. 2023; Nanayakkara et al. 2024; Park et al. 2024; Setton et al. 2024; Slob et al. 2024; Carnall et al. 2024), and can provide insight into the relative importance of fast (~ 100 Myr) and slow (~ 1 Gyr) quenching processes. Additionally, many studies have found that a large fraction of quiescent galaxies at $z > 2$ shows evidence for AGN activity based on line ratio diagnostics (e.g. Belli et al. 2024; D'Eugenio et al. 2024; Bugiani et al. 2024), suggesting that AGN may play a role in quenching star formation, as discussed above.

Outflows of neutral gas, likely driven by AGN, are prevalent and have been proposed as a dominant quenching mechanism for massive galaxies in the early Universe (Davies et al. 2024; Wu 2025; Valentino et al. 2025). However, the role of AGN in quenching galaxies in the early Universe is still uncertain. There is some evidence that AGNs in local post-starburst galaxies may have been fueled by the same processes that caused the quenching, rather than the quenching being driven by AGN feedback (Lanz et al. 2022). Furthermore, Almaini et al. (2025) found no evidence for excess AGN activity in massive PSBs in the redshift range $1 < z < 3$. Instead, low average X-ray luminosities were found, consistent with weak AGN activity that traces the star formation rate.

To better understand the dominant quenching mechanisms at early epochs, we analyze a sample of 24 post-starburst and quiescent galaxies at redshifts $1 < z < 3$ from the JWST Early eXtragalactic Continuum and Emission Line Survey (EXCELS; Carnall et al. 2024). The outline of this paper is as follows. In Section 2, we describe our observations and methods. In Section 3, we discuss the physical properties and star formation histories of these galaxies, derived from full spectral fitting. We also explore the emission line properties of the sample. We discuss these results and propose possible quenching mechanisms in Section 4, and present our summary in Section 5. We assume a Kroupa (2001) stellar initial mass function and a flat ΛCDM cosmology where necessary with $\Omega_M = 0.3$, $\Omega_\Lambda = 0.7$, and $h = 0.7$.

2. OBSERVATIONS AND METHODS

2.1. *Photometry*

We make use of 11 deep photometric bands from *JWST*/PRIMER imaging (GO 1837; PI: Dunlop) and *HST* imaging from CANDELS (Grogin et al. 2011;

Koekemoer et al. 2011) for all of the galaxies in our sample (*JWST*/NIRCam filters F090W, F115W, F150W, F200W, F277W, F356W, F410M, and F444W; *HST* ACS filters F435W, F606W, and F814W). The photometric catalog will be presented in Maltby et al. (in prep), but in brief, the NIRCam F200W filter is used as the detection image. Fluxes are measured in 0.5 arcsec-diameter apertures using SOURCEEXTRACTOR (Bertin & Arnouts 1996). The photometry is corrected to the total flux with an aperture correction dependent on the PSF for each filter and using the F200W MAGBEST parameter from SOURCEEXTRACTOR (the total magnitude) applied to all the filters. We note that this is a different photometric catalog from the one used to select the original EXCELS sample. The original EXCELS photometric catalog uses the F356W band to select objects, uses 0.35 arcsec-diameter apertures, and uses the F356W FLUX_AUTO parameter from SOURCEEXTRACTOR to correct to the total flux. However, the results presented in this paper remain the same regardless of which catalog is used.

2.2. *Spectroscopy*

The galaxy sample presented in this work is selected from the *JWST* EXCELS spectroscopic survey (GO 3543; PIs: Carnall, Cullen; Carnall et al. 2024). The EXCELS sample selection is described in Carnall et al. (2024) and is briefly summarized below. The EXCELS survey is designed to obtain medium-resolution (R $\sim$ 1000) spectroscopy of galaxies in the *JWST* Public Release IMaging for Extragalactic Research (PRIMER) Ultra-Deep Survey (UDS) field. The 4 NIRSpec/MSA pointings include observations of massive quiescent galaxies selected from both the VANDELS survey UDS-HST selection catalog (McLure et al. 2018) and from PRIMER UDS imaging (GO 1837; PI: Dunlop; Dunlop et al. 2021). Each pointing was observed for approximately 4 hours with the G140M and G395M gratings, and about 5.5 hours with the G235M grating, using the NRSIRS2 readout pattern.

To reduce the data, we process the raw level 1 products from the Mikulski Archive for Space Telescopes using v1.17.1 of the *JWST* reduction pipeline[1] and the Calibration Reference Data System (CRDS) context jwst_1322.pmap. First, we use the default level 1 configuration, but turn on the advanced snowball rejection option. We also run the clean_flicker_noise step to account for the 1/f detector readout noise. We then run the default level 2 pipeline without the sky subtraction

---

[1] https://github.com/spacetelescope/jwst

step. Residual artifacts in the 2D calibrated spectra from each of the three exposures, taken at different nod positions, are manually flagged and masked before performing sky subtraction using custom code. Finally, we run the level 3 pipeline to obtain the combined 2D flux calibrated spectra. We use a custom optimal extraction of the 2D spectra (Horne 1986) to obtain the 1D spectra featured in this work (see Carnall et al. 2024).

A flux calibration must be applied to the spectra to account for slit losses and spectrophotometric calibration issues. We integrate the spectra through the filters that overlap with the spectral data and scale the spectra to the fluxes by applying the mean normalization factor derived from all photometric points. As we often only have two photometric filters overlapping with the available spectra, we do not account for wavelength-dependent slit losses at this stage. These effects are instead addressed during our full spectral fitting analysis, where we introduce parameters to model them, as described in Section 2.4. In the cases where multiple gratings are available, following Carnall et al. (2024), we use SPECTRES (Carnall 2017) to degrade the higher resolution grating to the lower resolution grating in the overlapping regions. We then scale the G140M spectra to the mean flux of the region overlapping with the G235M spectra, and compute the mean pixel values from both gratings. A compilation of all the spectra is shown in Appendix A.

2.3. *Sample selection*

From the EXCELS sample we select 24 galaxies within the redshift range $1 < z < 3$ that were identified as quiescent based on the VANDELS survey and PRIMER imaging (see Section 3 of Carnall et al. 2024). The VANDELS quiescent samples were selected based on the $z > 1$ rest-frame UVJ color criteria proposed by Williams et al. (2009). The quiescent sample from the PRIMER imaging was selected using a specific star-formation rate (sSFR) cut of sSFR $< 0.2/t_{\text{universe}}$. These two sample selection methods have been shown to be highly consistent (e.g. Carnall et al. 2018, Stevenson et al. in prep). Additionally, there is one galaxy included in the survey that was selected as a PSB via a super-color analysis (described below) that was not in either the VANDELS or PRIMER passive samples. We ensure that all of these galaxies have secure spectroscopic redshift measurements. We exclude one galaxy for which we were unable to get a reliable fit to the spectroscopic data (see Section 2.4). The majority of our sample is observed only with the G140M grating (18 galaxies), with three being observed only with G235M and three observed

with both gratings. The selection criteria and gratings used to select each source are listed in Table 1.

We further subdivide our sample by calculating "super-colors" following the methodology of Wild et al. (2014), which has been shown to cleanly separate post-starburst galaxies from the rest of the galaxy population when applied to broadband photometric data. This technique involves identifying three "super-colors" (or principal component amplitudes) that represent a wide variety of shapes: the first super-color determines how red the SED is, the second super-color determines the strength of the Balmer or 4000Å break, and the third super-color determines the shape around the Balmer or 4000Å break. The super-colors are a linear combination of the available photometric bands from *HST* and *JWST* that maximize the variance of model SEDs using a PCA. Super-colors are thus similar to traditional colors without forcing the data to fit model SEDs. Within "super-color space" boundaries can be drawn to separate post-starburst, quiescent, star-forming, and dusty star-forming galaxies. These boundaries have been spectroscopically verified at $z < 1.4$ (Maltby et al. 2016; Wilkinson et al. 2021). The super-color classifications for the PRIMER field will be presented in de Lisle et al. (in prep). Note that a different eigenbasis is used, as we are using *HST* and *JWST* filters, so the boundaries differ from those in Wild et al. (2014).

The super-color classifications for the galaxies in our sample are listed in Table 1 and shown in Figure 1. Twenty of our galaxies fall within the quiescent or post-starburst regions of the diagram, with three galaxies classified as star-forming lying close to the quiescent boundaries and one galaxy classified as a dusty star-forming galaxy. There are 11 galaxies that fall within the PSB region of the super-color diagram and 9 galaxies classified as quiescent. Throughout the paper, we use the term 'PSB' to refer to super-color-selected PSBs.

2.4. *Spectral Fitting*

We use the Bayesian spectral fitting code BAGPIPES (Carnall et al. 2018, 2019) to jointly fit our spectroscopic data and all available *HST* ACS and *JWST*/NIRCam photometry. Additionally, we make use of archival spectra from VANDELS (McLure et al. 2018; Pentericci et al. 2018; Garilli et al. 2021), observed with the VIMOS instrument. There are four galaxies in our sample (ID-101499, ID-55414, ID-91726, ID-93227) with VANDELS spectra that we fit in conjunction with the NIRSpec spectra. We bin the VANDELS spectra by 2 pixels and fit the wavelength range 5200Å to 9250Å, following Carnall et al. (2019). We note that the results remain consistent when not including the VANDELS spectra.
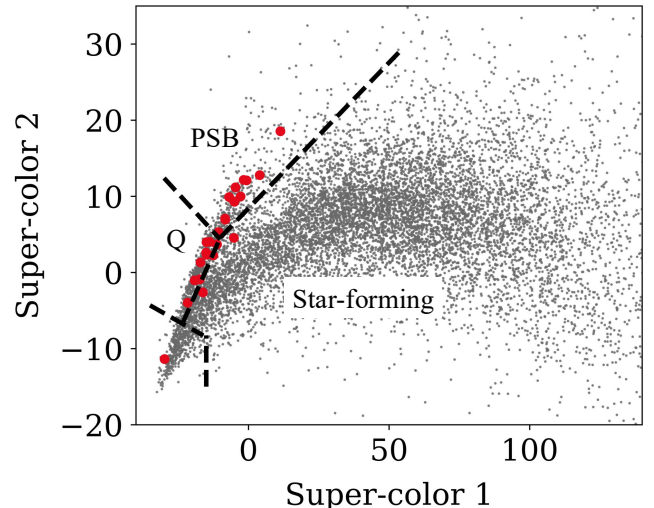

Figure 1. Super-color 1 (set by how red or blue the galaxy SED is) versus super-color 2 (determined by the strength of the 4000Å or Balmer break) based on photometry. Our sample of spectroscopically confirmed post-starburst and quiescent galaxies is shown in red and the underlying sample from the entire PRIMER field (de Lisle et al. in prep) is shown in gray. The dashed black lines indicate the boundaries between the post-starburst, quiescent, and star-forming regions.

Our priors (summarized in Table 2) are similar to those described in Carnall et al. (2024), apart from the SFH and dust model. We use the 2016 updated version of the Bruzual & Charlot (2003) spectral synthesis models, which uses the MILES stellar library (Sánchez-Blázquez et al. 2006; Falcón-Barroso et al. 2011). This library spans $3540 - 7350$Å, so we only fit our spectroscopic data within this range in rest-frame wavelengths. We mask regions of the spectra that may contain emission lines with a ± 5Å mask in the rest-frame. We include a nebular component with the ionization parameter fixed to $\log U = -3$. As done in Carnall et al. (2024), we include a 38th order Chebyshev polynomial to account for spectrophotometric calibration issues and slit losses. This is about 1 order per 100Å of rest-frame wavelength coverage, following the approach of Conroy & van Dokkum (2012) and Conroy et al. (2014). The priors on the redshifts are from the spectroscopic redshifts described in Carnall et al. (2024). To address the possibility of underestimating the observed uncertainties, we introduce a multiplicative factor on the error of the spectroscopic data, allowing it to vary from $1 - 10$. We use the nested sampling algorithm MULTINEST (Feroz et al. 2019) to sample the model posterior, which is accessed with the PYMULTINEST package (Buchner et al. 2014). We assume a Kroupa (2001) stellar initial mass function. We adopt the two-component dust attenuation model described in Wild et al. (2007), which assumes a fixed

EXCELS ID	z	Grating	$\log M^*/M_\odot$	Selection	SC class	Burst age (Gyr)	Lick Hδ_A (Å)	EW [OII] (Å)
101499	1.09	G140M	$10.25^{+0.05}_{-0.06}$	VANDELS	SF	$1.51^{+0.3}_{-0.5}$	$7.44^{+0.4}_{-0.4}$	$7.86^{+0.3}_{-0.4}$
114127	2.53	G235M	$10.56^{+0.05}_{-0.06}$	PRIMER	Q	$1.30^{+0.4}_{-0.3}$	$-$	$-$
114633	2.61	G140M	$10.54^{+0.06}_{-0.05}$	PRIMER	PSB	$0.69^{+0.1}_{-0.09}$	$6.47^{+0.5}_{-0.5}$	$2.66^{+2}_{-0.6}$
114929	2.18	G140M	$11.18^{+0.03}_{-0.04}$	PRIMER	SF (dusty)	$1.64^{+0.3}_{-0.5}$	8.45^{+1}_{-1}	6.77^{+2}_{-2}
122839	1.41	G140M	$10.87^{+0.04}_{-0.03}$	VANDELS	SF	$1.68^{+0.2}_{-0.5}$	$-$	$-$
123852	2.52	G140M	$10.82^{+0.04}_{-0.05}$	PRIMER	SF	$1.65^{+0.2}_{-0.4}$	$-$	28.03^{+1}_{-1}
127460	2.53	G140M/G235M	$10.85^{+0.03}_{-0.03}$	PRIMER	PSB	$0.52^{+0.1}_{-0.1}$	$7.05^{+0.3}_{-0.3}$	$6.44^{+0.4}_{-0.4}$
43944	2.30	G235M	$10.51^{+0.06}_{-0.04}$	PRIMER	PSB	$1.28^{+0.4}_{-0.2}$	$-$	$-$
54835	2.48	G140M	$10.78^{+0.03}_{-0.03}$	PRIMER	Q	$0.51^{+0.1}_{-0.2}$	$10.48^{+0.4}_{-0.3}$	10.85^{+2}_{-2}
55414	1.47	G140M	$11.04^{+0.05}_{-0.05}$	VANDELS	Q	$1.57^{+0.3}_{-0.2}$	$0.76^{+0.2}_{-0.3}$	$1.14^{+0.3}_{-0.4}$
60232	1.09	G140M	$10.19^{+0.05}_{-0.04}$	VANDELS	Q	$1.82^{+0.1}_{-0.2}$	$-$	$-$
63089	2.09	G140M/G235M	$10.55^{+0.06}_{-0.05}$	PRIMER	Q	$0.68^{+0.2}_{-0.1}$	$4.12^{+0.4}_{-0.3}$	0.00^{+0}_{-0}
63832	2.32	G140M	$10.86^{+0.04}_{-0.04}$	PRIMER	PSB	$0.83^{+0.1}_{-0.1}$	$4.32^{+0.4}_{-0.3}$	$1.98^{+2}_{-0.9}$
65234	2.23	G140M/G235M	$10.18^{+0.03}_{-0.03}$	PRIMER	PSB	$0.45^{+0.08}_{-0.07}$	$9.34^{+0.3}_{-0.3}$	$-$
69069	2.15	G140M	$10.33^{+0.04}_{-0.04}$	PRIMER	PSB	$0.53^{+0.1}_{-0.1}$	$7.75^{+0.4}_{-0.4}$	0.00^{+0}_{-0}
69759	1.53	G140M	$11.36^{+0.03}_{-0.03}$	VANDELS	Q	$1.67^{+0.2}_{-0.3}$	$-0.84^{+0.5}_{-0.4}$	$-$
72186	2.32	G140M	$10.96^{+0.02}_{-0.02}$	PRIMER	PSB	$1.01^{+0.08}_{-0.08}$	$6.02^{+0.2}_{-0.2}$	$1.77^{+0.2}_{-0.2}$
90549	1.09	G140M	$10.45^{+0.06}_{-0.07}$	VANDELS	Q	$1.76^{+0.2}_{-0.3}$	$-$	$-$
90591	1.09	G140M	$10.15^{+0.05}_{-0.05}$	VANDELS	PSB	$0.84^{+0.2}_{-0.1}$	$-$	$-$
91726	1.10	G140M	$10.85^{+0.03}_{-0.04}$	VANDELS	Q	$1.58^{+0.3}_{-0.2}$	$0.91^{+0.3}_{-0.2}$	$10.24^{+0.2}_{-0.2}$
93227	1.09	G140M	$10.45^{+0.05}_{-0.06}$	VANDELS	Q	$1.26^{+0.2}_{-0.2}$	$1.74^{+0.2}_{-0.2}$	$2.83^{+0.2}_{-0.2}$
94982	1.83	G140M	$10.97^{+0.03}_{-0.02}$	SC PSBs	PSB	$0.84^{+0.05}_{-0.07}$	$6.30^{+0.1}_{-0.1}$	$2.23^{+0.1}_{-0.1}$
97765	2.29	G140M	$10.45^{+0.03}_{-0.03}$	PRIMER	PSB	$0.79^{+0.08}_{-0.1}$	$3.84^{+0.3}_{-0.3}$	$1.75^{+0.6}_{-1}$
98447	2.81	G235M	$11.34^{+0.02}_{-0.02}$	PRIMER	PSB	$0.28^{+0.09}_{-0.08}$	$-$	$-$

Table 1. Measured properties of our sample of galaxies. The stellar masses and burst ages come from Bagpipes. The selection indicates how the galaxy was chosen, as described in Section 2.3. The SC class denotes the super-color classification based on photometry (see Section 2.3), where galaxies are classified as post-starburst (PSB), quiescent (Q), or star-forming (SF). We define Hδ_A as positive for absorption, while the equivalent width of [OII] is defined as positive in emission.

power-law exponent of $n = 0.7$ for the wavelength dependence of dust attenuation in the interstellar medium (ISM). Stars that are younger than 10 Myr have a fixed slope of $n = 1.3$ and are assumed to be more attenuated by a factor of η (modeled with a Gaussian prior) due to the birth clouds surrounding the stars.

We assume the two-component parametric SFHs described in Wild et al. (2020). The star formation rate as a function of time is given by

$$\psi(t) \propto \left. \frac{1 - f_{\rm burst}}{\int \psi_e {\rm d}t} \times \psi_e(t) \right|_{t_{\rm form} > t > t_{\rm burst}} \\ + \frac{f_{\rm burst}}{\int \psi_e {\rm d}t} \times \psi_{\rm burst}(t). \tag{1}$$

In addition to a double power-law component $\psi_{\rm burst}(t)$, this SFH also includes an exponential decay component $\psi_e(t)$ to account for older stellar populations. The parameter $f_{\rm burst}$ determines the fraction of mass formed during the starburst, and $t_{\rm form}$ denotes the lookback time when the older component started to form. The burst age $t_{\rm burst}$ is defined as the time since the peak of

the starburst. The two components are described by

$$\psi_e(t) = \exp^{\frac{-t}{\tau_e}} \tag{2}$$

and

$$\psi_{\rm burst}(t) = \left[\left(\frac{t}{t_{burst}} \right)^\alpha + \left(\frac{t}{t_{burst}} \right)^{-\beta} \right]^{-1}. \tag{3}$$

The exponential decay timescale of the older population is denoted as $\tau_{\rm e}$, and α and β set the declining and rising slopes of the starburst. We set $\beta = 250$, which is a typical value found for younger starbursts, as the variable β was found to be poorly constrained and had no impact on the results (Wild et al. 2020; Leung et al. 2024).

The free parameters and their corresponding priors of our Bagpipes model are summarized in Table 2. Errors on the properties derived from Bagpipes are calculated as the 16th to 84th percentile range. An example of one of the Bagpipes fits for a galaxy in our sample with a burst age of $0.84^{+0.05}_{-0.07}$ Gyr and a redshift of $z = 1.83$ is shown in Figure 2.

Model Component	Parameter	Range	Prior
SFH	$\log_{10}(M_*/M_\odot)$	(9,13)	Uniform
	t_{form} / Gyr	(0.4, 8)	Uniform
	τ_e / Gyr	(0.3, 10)	Uniform
	t_{burst} / Gyr	(0,2)	Uniform
	f_{burst}	(0, 1)	Uniform
	α	(0.01, 1000)	Logarithmic
	β	250	–
Metallicity	Z / $Z_\odot$	(0.01, 2.5)	Logarithmic
Dust	A_V / mag	(0,2)	Uniform
	Birthcloud factor η	(1,4)	Gaussian ($\mu = 3$, $\sigma = 1$)
Noise	White noise scaling a	(1,10)	Logarithmic
Miscellaneous	Redshift	$(z_{spec} \pm 0.01)$	Gaussian
	σ/km s^{-1}	(40, 500)	Logarithmic

Table 2. Model priors used for BAGPIPES fitting, as described in Section 2.4. All logarithmic priors are defined in base 10.
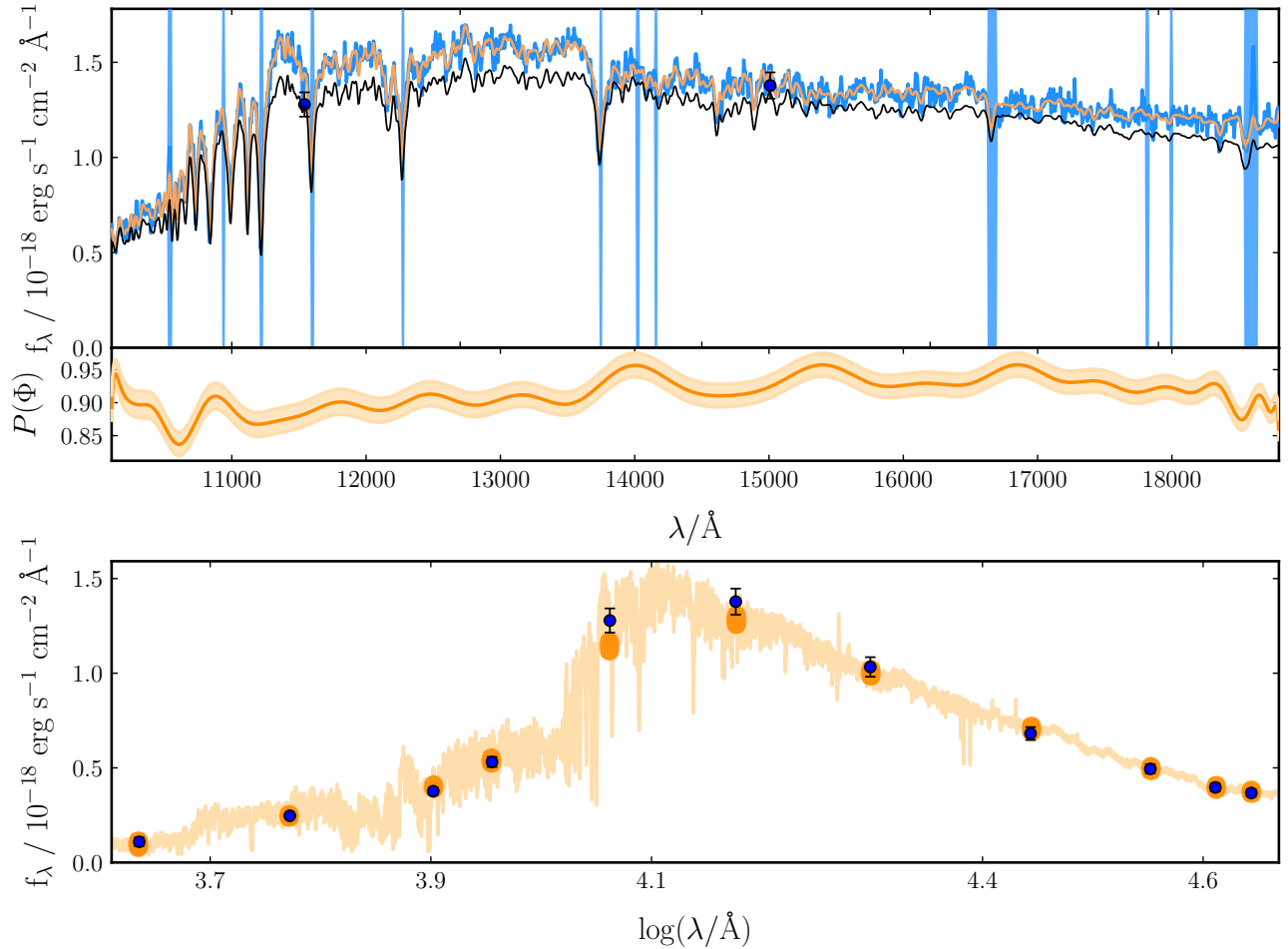
Figure 2. Example BAGPIPES fit of a post-starburst galaxy at $z = 1.83$ (EXCELS – 94982). *Top:* The input spectrum is shown in blue and the posterior fit is shown in orange. The photometric measurements are shown as blue points and the black line denotes the fitted model without calibration corrections. The blue shading indicates regions masked during fitting. The lower panel shows the spectrophotometric calibration component. *Bottom:* The input photometry is shown as blue points, the posterior fitted photometry is shown in orange, and the orange line shows the posterior SED.

2.5. *Spectral line fitting*

To obtain emission line fluxes, we use the Penalized PiXel-Fitting (pPXF) method (Cappellari 2023), which is upgraded from Cappellari (2017) and originally described in Cappellari & Emsellem (2004). We use templates from the Flexible Stellar Population Synthesis (FSPS; Conroy et al. 2009; Conroy & Gunn 2010) models. We perform an initial fit with an additive Legendre polynomial of degree 10 to obtain the stellar velocity and velocity dispersion. If there are multiple gratings, we set the instrumental resolution of the overlapping region to be the mean of the instrumental resolution. We then perform a fit optimized to the gas component, holding the stellar velocity and velocity dispersion constant. The gas is modeled as a single kinematic component. For this fit, we only include a multiplicative Legendre polynomial of degree 10.

The Lick Hδ_A index (Worthey & Ottaviani 1997) is often used to select for post-starburst galaxies (e.g. Chen et al. 2019; French 2021). We measure the Lick Hδ_A index for all galaxies with available wavelength coverage. Errors are estimated by adding random noise to each spectrum. This noise is uniformly distributed between -1 and 1 times the error spectra. We then recalculate Hδ_A for each perturbed spectrum. We also calculate the equivalent widths (EWs) of [OII]λ3727 and Hα, which are often used to select against current star formation (e.g. Chen et al. 2019; French 2021). We calculate these equivalent widths from the gaussian fits from pPXF. Errors are similarly calculated by perturbing each spectra with noise that is uniformly distributed between -1 and 1 times the error spectra. We repeat the fitting procedure described above and calculate the errors as the 16th and 84th percentiles. We list these measurements for our sample in Table 1.

3. RESULTS

3.1. *Star formation histories*

In Figure 3 we show the star formation rate (SFR) derived from BAGPIPES as a function of stellar mass for the 24 quiescent and post-starburst galaxies in our sample. All of the galaxies currently lie below the star-forming main sequence at $z = 2$ from Speagle et al. (2014), and the majority of the sample satisfies sSFR $< 0.2/t_{\mathrm{universe}}$, a common criteria in the literature for selecting quiescent galaxies (e.g. Pacifici et al. 2016; Carnall et al. 2024).

We show a montage of the star formation histories (SFHs) fitted by BAGPIPES for our sample of galaxies in Figure 4. The majority of our sample had high peak star formation rates ($\sim 100 - 1000$ M$_\odot$yr^{-1}), followed by rapid quenching and have low current star-formation
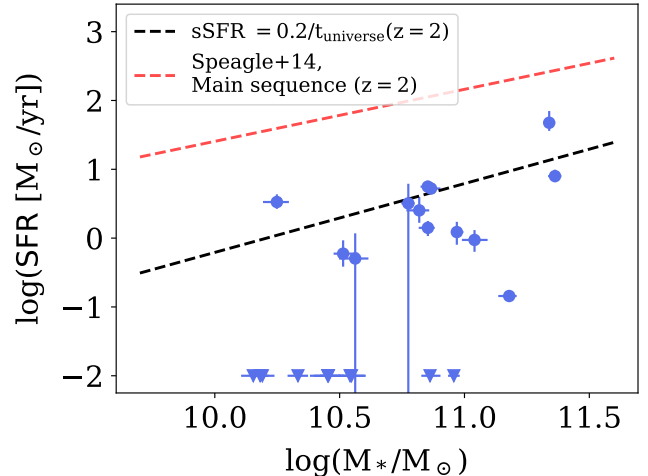

Figure 3. Star formation rate as a function of galaxy stellar mass, where both properties have been derived from our full spectral fitting analysis described in Section 2.4. Triangles indicate values that fall below log(SFR)< -2. The dashed black line indicates where sSFR $< 0.2/t_{\mathrm{universe}}$ at a redshift of $z = 2$. The dashed red line indicates the star-forming main sequence at $z = 2$ from Speagle et al. (2014).

rates. However, we observe a diverse range of SFHs. Some galaxies exhibit a well-defined burst of star formation followed by rapid quenching, while others appear to undergo a more prolonged period of star formation without a strong starburst. The star formation histories of $z \sim 1$ post-starburst galaxies presented in Wild et al. (2020) display a similar diversity to the SFHs found in this sample.

To assess the robustness of our conclusions to the choice of the SFH prior, we compare the SFHs derived here with those obtained using a double power-law prior following Carnall et al. (2024). The conclusions made throughout the paper remain the same when using a double power-law prior (the stellar mass, quenching timescales, and peak historical star formation rates are consistent within the errors). The exact duration of star formation for a few galaxies (e.g. EXCELS – 69759 and EXCELS – 114127) in our sample is poorly constrained due to large uncertainties in their SFHs, regardless of the prior.

3.2. *Super-colors*

In this section, we discuss the photometric classifications of our sample. We will use these classifications, based on photometry alone, to compare differences between our sample and the $z \sim 1$ galaxies in Wild et al. (2020). Understanding how well these photometric classifications work and their limitations is important, given that many galaxies lack spectroscopic data.
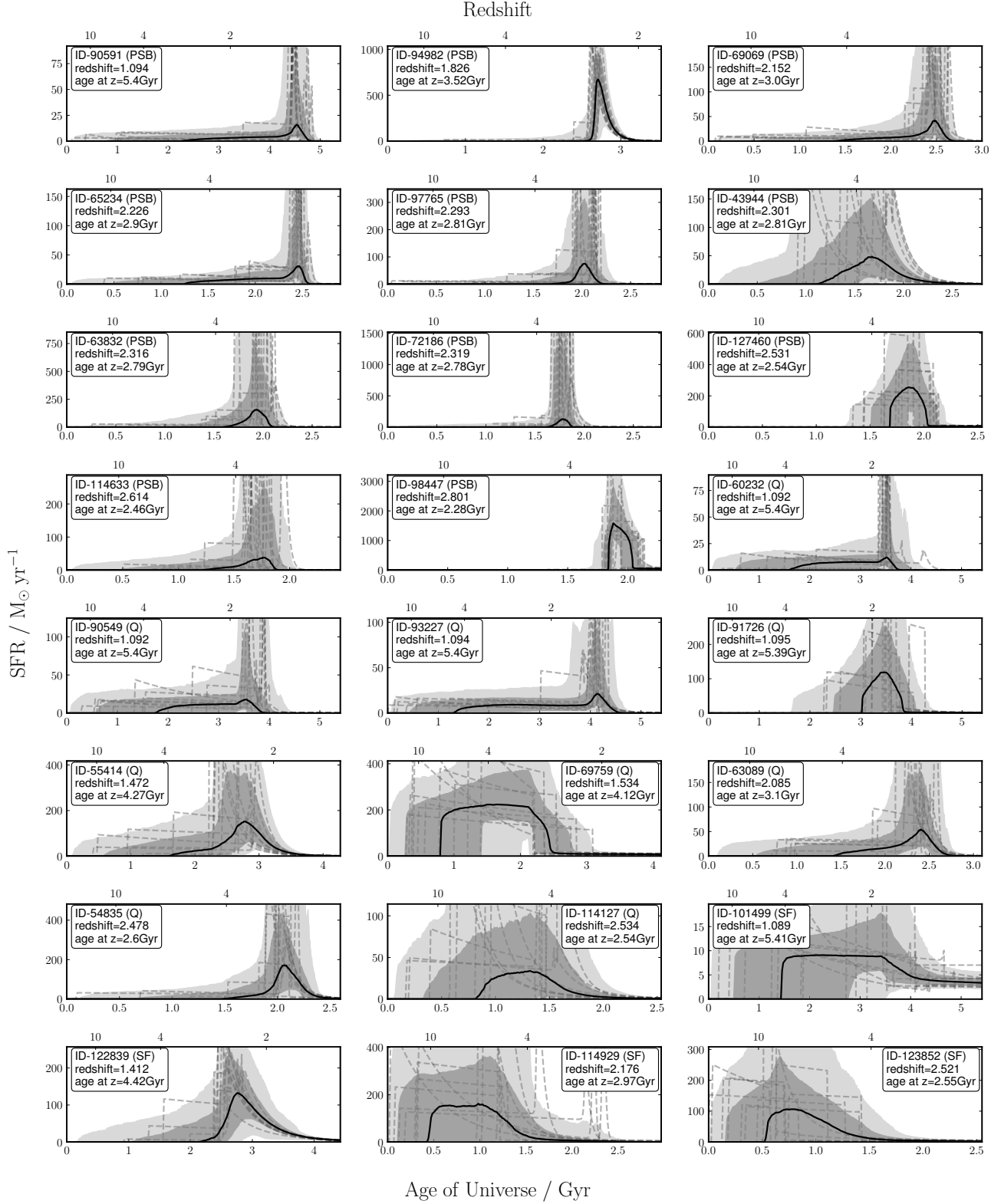
8

Figure 4. The star formation histories derived from BAGPIPES for the galaxies in our sample. The labels on each plot indicate the EXCELS-ID followed by its super-color classification (Q, PSB, SF), as described in Section 2.3. The black line indicates the median posterior in each age bin, the gray shading indicates the 68 percent confidence interval, and the light gray shading indicates the 95 percent confidence interval of the SFHs. The gray dashed lines show 10 random samples from the posterior distributions.

The criterion used in Wild et al. (2020) to select PSBs is H$\delta_A > 5$Å and EW [OII]< 5Å. Of all the super-color selected PSBs in our sample with wavelength coverage of Hδ_A and [OII], all but two satisfy H$\delta_A > 5$Å (but all satisfying H$\delta_A > 3.8$Å) and all but one satisfy EW [OII]< 5Å (but all satisfying EW [OII]< 6.5Å). Thus, the only galaxies in the PSB region that do not satisfy the criterion in used in Wild et al. (2020) are close to the limits. Of the six super-color selected quiescent galaxies with wavelength coverage of Hδ_A, one has H$\delta_A > 5$Å. Three of the five quiescent galaxies with wavelength coverage of [OII] have an EW [OII]< 5Å, with two having an EW [OII]> 10Å. One of these quiescent galaxies with a high EW [OII], one has H$\delta_A < 1$Å However, the other quiescent galaxy (EXCELS – 54835) has both a high Hδ_A and EW [OII], suggesting there is some contamination in the quiescent region based on traditional spectroscopic selection methods. This confirms for the first time that the super-color selected PSB and quiescent galaxies are robust above redshifts of $z \sim 1.4$ up to $z \sim 3$. Further investigation of the super-color selection method will be presented in de Lisle et al. (in prep), which will include a larger sample of ground-based spectra.

Figure 5 shows the burst ages (the time since the peak of the starburst) of the galaxies in super-color space, as derived using Bagpipes. The galaxies in the post-starburst region of the diagram tend to have younger burst ages than the galaxies falling in the quiescent region, as expected. The median burst age of galaxies is 0.8 Gyr within the post-starburst region, and 1.5 Gyr within the quiescent region. Within the post-starburst region, there is a tentative trend in burst age, with younger burst ages having higher super-color 1 and super-color 2, although we are limited by a small number of post-starburst galaxies. Such a trend is not present in the quiescent region of the diagram. Within the post-starburst region, we find that galaxies closer to the quiescent region with young burst ages have lower burst mass fractions. This may be due to the positive correlation between the burst age and the burst mass fraction, possibly resulting from high uncertainties in the burst mass fraction or from effects related to the degeneracy between the burst age and the mass (Leung et al. in prep). Such scatter between the burst age and the position in super-color space is expected due to the degeneracy between the burst age and burst mass fraction when relying on photometry alone (Wild et al. 2007).

Using the star formation histories derived from Bagpipes, we can predict how the galaxies in our sample move through super-color space. We generate mock photometry starting from the peak of the most recent burst
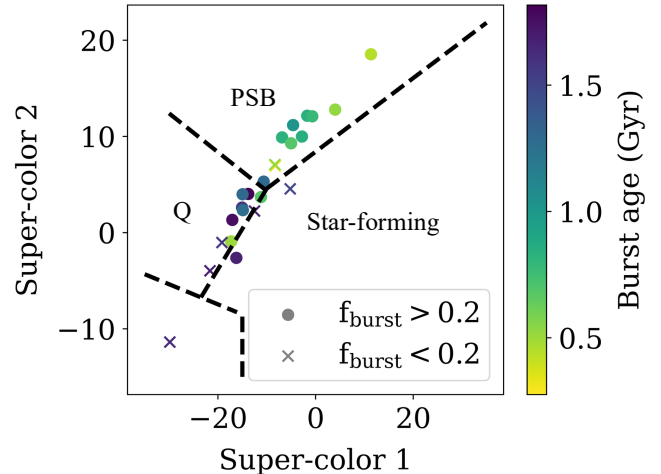

Figure 5. Super-color 1 versus super-color 2 based on photometry, as in Figure 1. The points are colored according to the burst age of the galaxy (defined as the time since the peak of the starburst) from Bagpipes. The size of the points indicates whether the burst mass fraction is greater or less than 0.2.

from the SFHs predicted by Bagpipes for all of our galaxies in redshift intervals of 0.1. We then calculate the super-color in each redshift interval such that the photometric bands cover the same wavelengths as those at the galaxy's observed spectroscopic redshift. We assume the observed dust attenuation of our galaxies does not change pre- and post-quenching when constructing these evolutionary tracks. We show the median "super-color tracks" of two of the galaxies in our sample (EXCELS – 94982 and EXCELS – 55414) in Figure 6. The post-starburst galaxy EXCELS – 94982 currently resides in the star-forming region of the super-color diagram, and after the burst of star formation begins climbing up towards the top of the post-starburst region. As star formation is nearly completely quenched, the galaxy moves towards the quiescent region of the diagram. The red star indicates the current position of the galaxy in super-color space, and the points below this redshift show the expected super-color values assuming no rejuvenation event occurs. In contrast, three of the quiescent galaxies in our sample (such as EXCELS – 55414) never enter the post-starburst region of the diagram.

Figure 7 shows the visibility time of post-starburst galaxies, defined as the amount of time spent in the post-starburst selection region in the super-color diagram, versus stellar mass. The median visibility time in our sample is 612 Myr, excluding six sources that never enter the PSB region and have a median visibility timescale of zero. We compare this timescale to those found in other studies in Section 4.1. We perform a linear least-squares regression between the visibility time and stellar
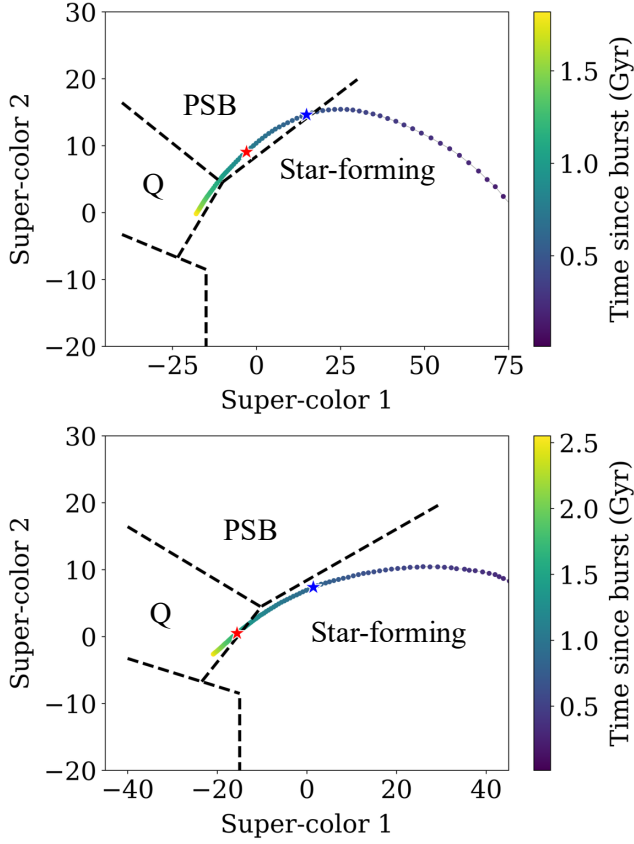
Figure 6. Change in super-colors over time based on the star-formation history from BAGPIPES for EXCELS-94982 (top) and EXCELS-55414 (bottom). The red star indicates the current position of the galaxy in super-color space. The blue star indicates when the galaxy became quenched (sSFR $< 0.2/t_{\mathrm{universe}}$). The dashed black lines indicate the boundaries between the post-starburst, quiescent, and star-forming regions, as in Figure 5.

mass and find that the Pearson correlation coefficient is $-0.42^{+0.08}_{-0.09}$ with a p-value of $0.08^{+0.08}_{-0.05}$ (corresponding to a 1.8σ significance), suggesting that there is a tentative trend.

3.3. Line diagnostics

Here we explore the ionized gas in our sample of quenching and quenched galaxies. In the top panel of Figure 8, we show the BPT diagram (Baldwin et al. 1981) of the [NII]/Hα versus [OIII]/Hβ line ratios. There are eight galaxies with wavelength coverage of all four emission lines, where at least one emission line in each ratio is detected at $> 3\sigma$. We include upper and lower detection limits when only one line is detected in either of the line ratios. We show the theoretical limit separating AGNs and starbursts from Kewley et al. (2001), as well as the redshift-dependent classification line proposed by Kewley et al. (2013). We also show
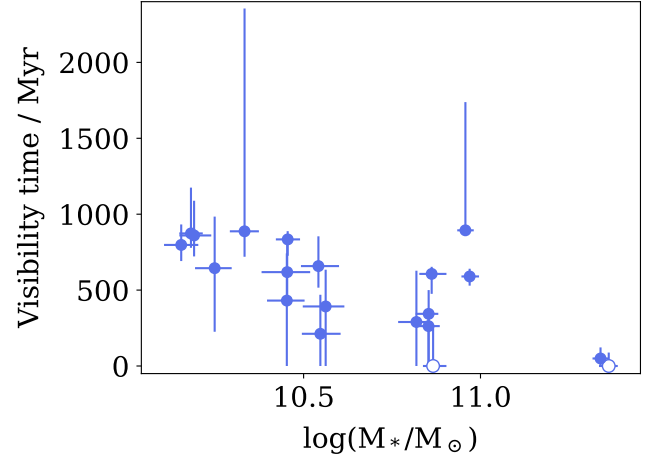
Figure 7. The visibility time of galaxies spent in the post-starburst region of the super-color diagram versus stellar mass. Open circles indicate galaxies that have a median visibility time of zero, but enter the PSB region within the uncertainty. We find a median visibility time of 612 Myr.

the star formation limit derived by Kauffmann et al. (2003b) based on a sample of nearby galaxies from the Sloan Digital Sky Survey. The majority of galaxies with robust line ratios fall into the AGN region of the BPT diagram. We also plot the distribution of local galaxies based on the DR8 MPA-JHU measurements[2] from the SDSS survey (Kauffmann et al. 2003a; Brinchmann et al. 2004; Tremonti et al. 2004). Our sample is clearly offset from the local star-forming sequence, with higher values of [NII]/Hα.

We show the WHaN diagnostic diagram proposed by Cid Fernandes et al. (2010, 2011) in the bottom panel of Figure 8. This diagram is useful in distinguishing ionization from weak AGN and 'retired galaxies' (which are not forming stars and are ionized by hot evolved stars) in the absence of [OIII] and Hβ (Cid Fernandes et al. 2011). The criterion $\log([\mathrm{NII}]/\mathrm{H}\alpha) > -0.4$ is sometimes used to indicate non-stellar photoionization. Thirteen of the fifteen galaxies in our sample satisfy this condition (with two lacking robust detections for either line). However, as shown in the bottom panel of Figure 8, about half of the galaxies with detections have an $\mathrm{EW}_{H\alpha} < 3$Å, which Cid Fernandes et al. (2011) suggest are likely quenched galaxies with older stellar populations. We emphasize that this limit is likely conservative, given that this limit was designed for the local Universe and stellar populations tend to be younger at higher redshifts. The galaxies above (below) this limit are shown in blue (orange) in Figure 8. Combined with classifications from the BPT

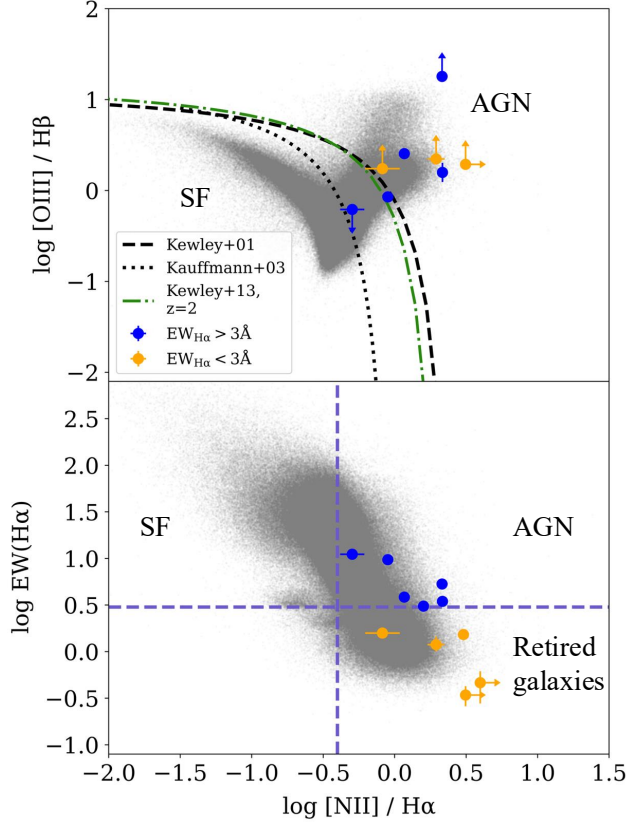
[2] https://www.sdss4.org/dr17/spectro/galaxy_mpajhu/

Figure 8. *Top:* BPT diagram for our sample of post-starburst and quiescent galaxies. Galaxies with an $EW_{H\alpha} > 3Å$ are shown in blue and galaxies with an $EW_{H\alpha} < 3Å$ are shown in orange. The gray points show the distribution of local galaxies from SDSS (Kauffmann et al. 2003a; Brinchmann et al. 2004; Tremonti et al. 2004). *Bottom:* WHaN diagram for our sample of post-starburst and quiescent galaxies. The lavender dashed lines indicate the separation between AGN, star-forming galaxies, and retired galaxies proposed by Cid Fernandes et al. (2011).

diagram described above, four of the eight galaxies with robust line detections meet the AGN criteria in both diagnostics. These four galaxies are on the higher mass end of the sample ($\log M_*/M_\odot > 10.8$) and have higher star formation rates. The measured BPT and WHaN diagnostics are summarized in Table 3. We will further investigate whether there is AGN activity in Section 4.4.

4. DISCUSSION

In this paper, we present a sample of $z \sim 2$ quenching and quenched galaxies. In this section, we explore the visibility timescales of PSBs, their possible progenitors, and discuss the implications of the quenching timescales of these galaxies. Finally, we discuss the role AGN may be playing in quenching at cosmic noon. We summa-

rize the relevant parameters discussed in this section in Table 4.

4.1. Visibility times

The visibility timescales of PSBs can be used to constrain the importance of PSBs for the growth of the quiescent galaxy population (e.g. Wild et al. 2016; Taylor et al. 2023). The visibility times found in this sample (see Section 3.2) have a similar range to the post-starburst visibility times found by Wild et al. (2020) with a sample of galaxies at $0.5 < z < 1.3$, and show no evidence for evolution in visibility times up to $z \sim 3$. This might suggest that the same physical mechanism(s) are responsible for quenching star formation at $z \sim 1$ and $z \sim 2$. Additionally, we find a tentative trend between the visibility time and stellar mass (a 1.8σ trend, see Section 3.2), although this is over a narrow range of stellar masses and we are limited by a small sample. In other papers that also define PSBs using super-colors, the PSB visibility timescale is estimated by different methods. de Lisle et al. (in prep) calculate visibility times by comparing mass functions of post-starburst and quiescent galaxies at different epochs and find that visibility times get shorter with increasing stellar mass between $10^9 M_\odot$ and $10^{10} M_\odot$, but with no clear trend at higher masses. Harrold et al. (in prep) calculate the visibility times of PSBs using semi-analytic models, and find a tentative trend with visibility times getting shorter with increasing stellar mass between $10^{9.5} M_\odot$ and $10^{11.5} M_\odot$.

Taylor et al. (2023) found that PSBs may account for about 50% of the growth of the massive ($\log M_*/M_\odot > 10.7$) quiescent galaxy population, and potentially all the growth at lower masses, at $z \sim 2$ assuming a visibility time of 500 Myr. If the visibility times are longer, the contribution of PSBs to the growth of the quiescent galaxy population would be lower, making them a less dominant pathway. Taking the 20% longer visibility time that we measure from our sample decreases this estimate to PSBs contributing about 40% to the growth of the quiescent galaxy population. However, when splitting by mass, the median visibility time of ~ 340 Myr at $\log M_*/M_\odot > 10.7$ increases the estimated contribution of PSBs to the growth of the massive quiescent galaxy population to $\sim 73\%$. The longer median visibility time of ~ 660 Myr at $\log M_*/M_\odot < 10.7$ allows for some of the growth of the quiescent sequence via galaxies that do not undergo a post-starburst phase. Thus, PSBs are an important pathway in the growth of quiescent galaxies at $z \sim 2$.

4.2. Progenitors of quenched galaxies at cosmic noon

EXCELS ID	EW Hα (Å)	log([NII]/Hα)	log([OIII]/Hβ)
101499	$11.09^{+0.4}_{-0.4}$	-0.296 ± 0.085	< -0.209
93227	$0.34^{+0.08}_{-0.08}$	> 0.496	> 0.287
91726	$9.69^{+0.1}_{-0.1}$	-0.048 ± 0.015	-0.070 ± 0.059
114633	–	–	> 0.180
123852	–	–	> 0.580
97765	–	–	not detected
127460	$3.46^{+0.1}_{-0.1}$	0.335 ± 0.010	0.198 ± 0.105
98447	0.00^{+0}_{-0}	> 1.735	not detected
114929	–	–	not detected
114127	$1.19^{+0.3}_{-0.2}$	0.290 ± 0.060	> 0.346
69069	–	–	> 0.308
54835	–	–	> 0.303
63832	–	–	> 0.375
43944	$3.07^{+0.3}_{-0.3}$	0.202 ± 0.032	–
72186	–	–	not detected
63089	0.00^{+2e-17}_{-0}	–	not detected
65234	$0.46^{+0.2}_{-0.2}$	> 0.599	not detected
94982	$1.53^{+0.09}_{-0.09}$	0.481 ± 0.015	not detected
90591	$0.00^{+0.1}_{-0}$	> 0.431	not detected
122839	$3.84^{+0.1}_{-0.1}$	0.068 ± 0.028	0.406 ± 0.046
90549	$0.42^{+0.1}_{-0.2}$	not detected	> 0.102
69759	$5.31^{+0.2}_{-0.2}$	0.332 ± 0.012	> 1.255
60232	0.00^{+0}_{-0}	not detected	not detected
55414	$1.58^{+0.2}_{-0.1}$	-0.085 ± 0.121	> 0.240

Table 3. Measurements for fitted emission lines. The equivalent width of Hα is defined as positive for emission. The line ratios log([NII]/Hα) and log([OIII]/Hβ) are labeled as 'not detected' if both emission lines are undetected at $> 3\sigma$. Dashes indicate the the lines were not observed.

Submillimeter galaxies (SMGs) have been suggested as possible progenitors of post-starburst galaxies (e.g. Almaini et al. 2017; Wild et al. 2020; Wilkinson et al. 2021). To investigate this possibility, we examine the peak historical SFR derived from BAGPIPES for our sample as a function of the redshift at which this occurs in Figure 9. The range of historical maximum SFRs (16-4695 $M_{\odot}yr^{-1}$) is consistent with those found in Wild et al. (2020) for $z \sim 1$ PSBs. Note that for the historical maximum SFRs of the Wild et al. (2020) sample we consider the peak of the recent starburst, which is slightly lower for a few galaxies that did not have a strong recent starburst. The range of SFRs of SMGs found by Swinbank et al. (2014) is $20 - 1030$ $M_{\odot}yr^{-1}$, which is consistent with the SFRs achieved by all but one of the galaxies in our sample. SMGs have been found to have stellar masses and space densities consistent with them being the progenitors of post-starburst galaxies (Wilkinson et al. 2021).

To investigate whether the galaxies in our sample are the descendants of SMGs, we consider the sample of SMGs presented in Gillman et al. (2024). There are sixteen galaxies in our sample that have SFRs that exceed 200 $M_{\odot}yr^{-1}$ in the redshift range of the Gillman et al. (2024) sample ($1.4 < z < 4.6$). We assume that our lower limit of 200 $M_{\odot}yr^{-1}$ roughly corresponds to the ALMA 870 μm $S_{870m} = 2$ mJy (e.g. Hayward et al. 2011). Considering the number density of sources in the Gillman et al. (2024) sample within the UDS field, and the number density of sources in our sample likely to have undergone an SMG phase (assuming our sample is representative of the parent sample in the EXCELS footprint), we find that our sample has a density $\sim 7\times$ higher than that of the SMGs. However, SMGs are visible for much shorter time scales. Based on our predicted SFHs, our galaxies only exceed SFRs of 200 $M_{\odot}yr^{-1}$ for around 70 Myr, which is about ~ 7 times shorter than the time our galaxies have been visible as post-starburst or quiescent. Thus, based on these number densities and visibility times, SMGs are likely progenitors of the galaxies in our sample.

Additionally, post-starburst galaxies have been found to be compact at $z > 1$ (e.g. Almaini et al. 2017; Ji et al. 2024), consistent with the compact sub-millimeter

EXCELS ID	$\mathrm{SFR_{max}}(\mathrm{M_\odot/yr})$	$z_{\mathrm{SFR_{max}}}$	Visibility time (Myr)	τ_{q1} (Gyr)	$t_{50} - t_{90}$ (Gyr)
101499	16^{+14}_{-4}	4.0^{+5}_{-2}	644^{+340}_{-419}	2.59^{+1}_{-1}	$1.71^{+0.6}_{-0.5}$
114127	295^{+358}_{-181}	$4.9^{+2}_{-0.9}$	392^{+242}_{-392}	$0.60^{+0.2}_{-0.5}$	$0.31^{+0.2}_{-0.2}$
114633	1190^{+1361}_{-710}	$3.5^{+0.2}_{-0.2}$	658^{+196}_{-142}	$0.06^{+0.1}_{-0.04}$	$0.04^{+0.1}_{-0.03}$
114929	674^{+5708}_{-375}	$5.4^{+13.0}_{-1.2}$	0^{+0}_{-0}	$0.49^{+0.7}_{-0.4}$	$0.39^{+0.4}_{-0.3}$
122839	241^{+66}_{-112}	$2.4^{+0.2}_{-0.2}$	0^{+260}_{-0}	$1.58^{+0.2}_{-0.4}$	$0.66^{+0.1}_{-0.1}$
123852	278^{+224}_{-141}	$8.4^{+10.4}_{-2.5}$	290^{+338}_{-290}	$0.85^{+0.2}_{-0.4}$	$0.42^{+0.1}_{-0.2}$
127460	383^{+672}_{-170}	$3.6^{+0.4}_{-0.2}$	263^{+90}_{-263}	$0.34^{+0.3}_{-0.2}$	$0.14^{+0.1}_{-0.1}$
43944	265^{+46}_{-114}	$4.0^{+1}_{-0.4}$	0^{+0}_{-0}	$0.72^{+0.1}_{-0.1}$	$0.31^{+0.08}_{-0.05}$
54835	576^{+742}_{-255}	$3.1^{+0.2}_{-0.2}$	0^{+0}_{-0}	$0.35^{+0.2}_{-0.3}$	$0.16^{+0.1}_{-0.09}$
55414	508^{+217}_{-258}	$2.4^{+0.3}_{-0.2}$	0^{+0}_{-0}	$0.87^{+0.2}_{-0.2}$	$0.39^{+0.3}_{-0.06}$
60232	130^{+281}_{-98}	$1.8^{+0.07}_{-0.1}$	860^{+229}_{-138}	$0.11^{+0.3}_{-0.07}$	$0.60^{+0.8}_{-0.6}$
63089	358^{+693}_{-182}	$2.7^{+0.2}_{-0.2}$	212^{+257}_{-212}	$0.21^{+0.3}_{-0.2}$	$0.21^{+0.4}_{-0.2}$
63832	2042^{+2649}_{-1112}	$3.2^{+0.2}_{-0.1}$	607^{+47}_{-131}	$0.08^{+0.2}_{-0.05}$	$0.05^{+0.1}_{-0.03}$
65234	241^{+253}_{-111}	$2.6^{+0.08}_{-0.06}$	873^{+302}_{-95}	$0.08^{+0.1}_{-0.05}$	$0.19^{+0.2}_{-0.2}$
69069	331^{+470}_{-155}	$2.6^{+0.1}_{-0.09}$	887^{+1468}_{-168}	$0.12^{+0.3}_{-0.08}$	$0.12^{+0.2}_{-0.1}$
69759	317^{+204}_{-81}	6.9^{+8}_{-3}	0^{+88}_{-0}	$1.71^{+0.6}_{-0.7}$	$0.78^{+0.3}_{-0.3}$
72186	4695^{+3947}_{-2758}	$3.5^{+0.1}_{-0.1}$	894^{+845}_{-29}	$0.06^{+0.1}_{-0.04}$	$0.02^{+0.06}_{-0.01}$
90549	274^{+520}_{-197}	$1.8^{+0.08}_{-0.1}$	618^{+194}_{-195}	$0.12^{+0.3}_{-0.07}$	$0.48^{+0.8}_{-0.4}$
90591	138^{+156}_{-69}	$1.4^{+0.06}_{-0.06}$	798^{+135}_{-106}	$0.15^{+0.3}_{-0.1}$	$0.23^{+0.9}_{-0.2}$
91726	198^{+286}_{-95}	$2.1^{+0.4}_{-0.2}$	344^{+156}_{-344}	$0.78^{+0.7}_{-0.5}$	$0.31^{+0.3}_{-0.2}$
93227	179^{+344}_{-112}	$1.5^{+0.09}_{-0.08}$	431^{+311}_{-431}	$0.24^{+0.5}_{-0.2}$	$0.62^{+0.9}_{-0.6}$
94982	1004^{+94}_{-164}	$2.4^{+0.05}_{-0.05}$	590^{+51}_{-61}	$0.51^{+0.05}_{-0.06}$	$0.17^{+0.02}_{-0.02}$
97765	623^{+1096}_{-333}	$3.1^{+0.1}_{-0.1}$	834^{+54}_{-108}	$0.11^{+0.2}_{-0.08}$	$0.06^{+0.1}_{-0.05}$
98447	1867^{+1405}_{-631}	$3.4^{+0.08}_{-0.05}$	50^{+73}_{-50}	$0.21^{+0.1}_{-0.1}$	$0.09^{+0.04}_{-0.04}$

Table 4. Measured properties of our galaxy sample, with values given as posterior medians and errors derived from the 16th and 84th percentiles of the BAGPIPES posterior distributions. The columns are (1) EXCELS ID number, (2) the maximum historical star formation rate, (3) the redshift this star formation rate is achieved, (4) the time that galaxies remain in the super-color post-starburst selection region, (5) the time from peak star formation to sSFR$= 0.2/t_{\mathrm{H}}$, where t_{H} is the Universe's age at the time of quenching, (6) the time to grow from 50% to 90% of the total stellar mass.

sizes from ALMA, although the rest-frame optical sizes of SMGs are $\sim 2 - 4$ times larger (Simpson et al. 2015; Lang et al. 2019). All of the galaxies in our sample exhibit extremely compact morphologies with a median effective radius of ~ 1.1 kpc (Maltby et al. in prep), further supporting the idea that these galaxies may be the descendants of SMGs.

4.3. Quenching timescales

Different quenching timescales can be used to probe various quenching mechanisms. Figure 10 shows the quenching timescale τ_{q1} as a function of stellar mass. The quenching timescale τ_{q1} is defined as the amount of time from peak star formation to sSFR$= 0.2/t_{\mathrm{H}}$, where t_{H} denotes the Universe's age at the time of quenching. There are fifteen galaxies in our sample that quench within 500 Myr, six galaxies that quench between 500 Myr and 1 Gyr, and three galaxies that take longer than 1 Gyr to fully quench. The galaxies with the highest maximum SFRs tend to have the fastest quenching

times, possibly due to winds driven by star formation, star formation fueling an AGN, or gas depletion.

A large fraction of our sample has quenching times longer than those in Wild et al. (2020), which is due to our sample including quiescent galaxies. If PSBs become quiescent, then the quiescent sample should contain some galaxies with rapid quenching times, although the errors are expected to be larger as the star formation burst occurred longer ago. If there are some quiescent galaxies that do not have short quenching times, that allows for the other approximately 50% of quenched galaxies that do not go through a PSB phase, as predicted by Taylor et al. (2023). Of the nine quiescent galaxies in our sample, six have undergone a PSB phase in the past (based on the "super-color tracks" described in Section 3.2) of which four have quenched within 500 Myr. The other three quiescent galaxies never had a PSB phase.

We also consider a quenching timescale that is not dependent on the sSFR. The quenching time $t_{50} - t_{90}$ is defined as the time it takes a galaxy to grow from 50%
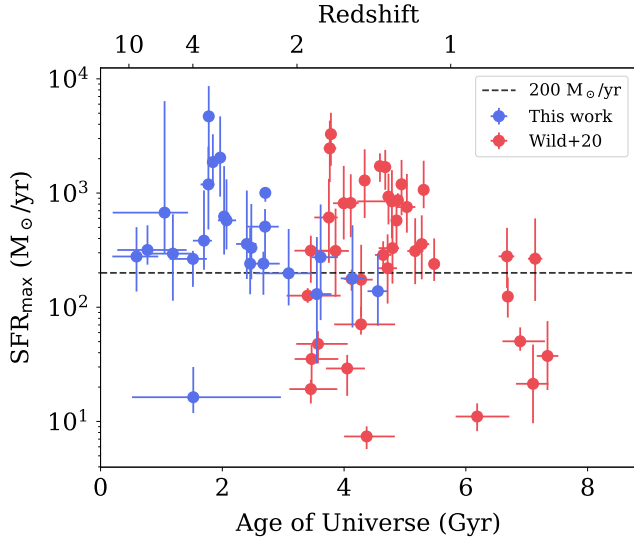
Figure 9. The peak historical star formation rate as a function of the age of the Universe when this occurred for galaxies in this sample and from the $z \sim 1$ Wild et al. (2020) sample. The dashed black line indicates a SFR of 200 $M_\odot yr^{-1}$, which we consider as a lower limit for SMGs.

to 90% of its total formed stellar mass. We see a range of quenching timescales, with faster quenching timescales more common at higher redshift, although this is partly due to the limited time available for galaxies to form and gradually quench when the Universe was so young. We note that the $t_{50} - t_{90}$ statistic is only appropriate as a quenching time measurement for galaxies which undergo a single episode of star formation, which is not consistent for galaxies with an extended SFH prior to the most recent starburst. Kimmig et al. (2025) find that most quenched galaxies in the MAGNETICUM simulations have quenching timescales of $t_{50} - t_{90} < 170$ Myr. There are eight galaxies in our sample with $t_{50} - t_{90} < 170$ Myr. However, many of the timescales found in this work and in Wild et al. (2020) are significantly longer, and are sometimes even longer than 1 Gyr. While MAGNETICUM is able to reproduce the observed number densities of quiescent galaxies at $z \sim 3 - 4$, they over-predict the number density of $z \sim 2$ quiescent galaxies likely due to an overly efficient AGN feedback model (Lagos et al. 2025). This may explain the very fast quenching times found by Kimmig et al. (2025).

The timescales we find in this work are broadly consistent with the wide range of quenching timescales found in other galaxy populations. Tacchella et al. (2022) find a wide range of quenching timescales (0-5 Gyr) based on the time it takes to transition from $sSFR < 1/[20 t_{universe}]$ to $sSFR < 1/[3 t_{universe}]$ in a sample of massive quiescent galaxies at $z \sim 0.8$. Samples of young quiescent galaxies at $z \sim 1.5$ that have un-

dergone a major starburst have quenching times around $\tau_{q1} \sim 300$ Myr (Park et al. 2023), which is longer than the median quenching time of ~ 116 Myr for post-starburst galaxies in this sample.

The diversity of quenching timescales we see in this sample suggest that these galaxies are being quenched by different processes. Studying the cold gas reservoirs in conjunction with the SFHs of quenching galaxies may shed light on quenching mechanisms. A simple explanation for slow quenching is gas starvation. In the local Universe, cutting off the supply of cold gas to galaxies may result in quenching timescales on the order of several Gyr (Schawinski et al. 2014; Peng et al. 2015). There is evidence that AGN activity may shorten quenching times (Wright et al. 2019), so a plausible explanation for our rapidly quenched galaxies ($\tau_{q1} < 500$) is gas exhaustion from a major starburst coupled with AGN feedback. Belli et al. (2019) find that galaxies that quench rapidly likely undergo a compaction event (i.e., a rapid buildup of a dense stellar core) due to their compact sizes and spheroidal morphologies followed by quenching due to gas exhaustion and stellar feedback. Compaction events may be triggered by processes such as major or minor mergers, counter-rotating streams, or tidal-compressions that result in an inflow episode (Zolotov et al. 2015). Our sample also has compact spheroidal galaxies with a median effective radius of 1.1 kpc and a median Sérsic index of $n = 3.6$ (Maltby et al. in prep), suggesting many of our galaxies have undergone compaction events prior to quenching.

We do not see a trend with the quenching time scales and stellar mass, possibly due to our small sample size. Looking at galaxies that are passive at $z = 0$ in the EA-GLE simulation, Wright et al. (2019) find that there is a negative correlation between quenching timescales and mass at $\log M_*/M_\odot > 9.7$, although the environment of the galaxy likely also plays a role. Taylor et al. (2023) suggest that the environment could have an effect on quenching out to $z \sim 2$. It is possible that environmental effects are playing a role, but we defer a more detailed investigation of this to future work.

4.4. *The Presence of AGNs*

The role of AGN in quenching star formation in galaxies remains uncertain. Current simulations suggest that while gas consumption and stellar feedback cause the initial decline in the SFR, an additional mechanism such as AGN feedback must be invoked to completely quench the galaxy (Zheng et al. 2020). However, there is some evidence from simulations that the consumption of dense ISM gas following a merger, coupled with morphological quenching, is sufficient to halt star formation without
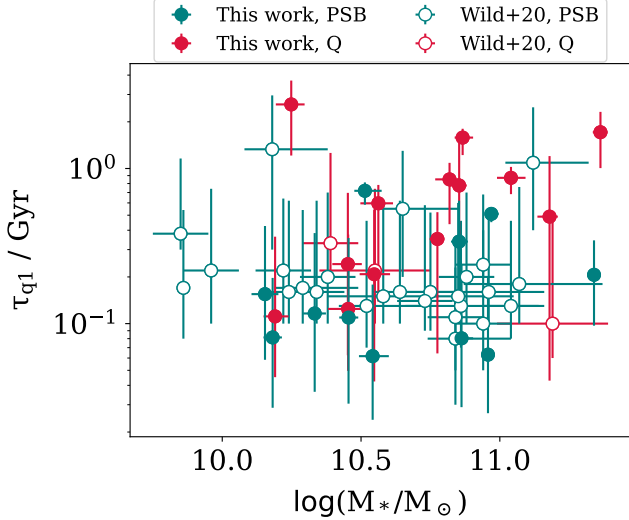
Figure 10. Quenching timescale as a function of stellar mass found for this sample of galaxies and those from Wild et al. (2020). The points are colored according to their super-color classification. We include the few galaxies classified as star-forming (but near the quiescent boundary) in the quiescent sample.

invoking AGN feedback (Petersson et al. 2023). Out of the five galaxies in our sample with reliable line ratios that satisfy EW(Hα) > 3Å, such that the ionization lines are likely not due to evolved stars (Cid Fernandes et al. 2011), four fall in the AGN region of the BPT diagram (see Figure 8). The BPT diagram is not able to distinguish between shocks driven by starbursts and photoionization due to an AGN (Kewley et al. 2019). However, the low SFRs present in these systems suggests that if shocks are responsible for the high BPT emission line ratios, they are unlikely to be driven by stellar feedback. While merger-induced shocks may also reproduce the emission line ratios of AGN in the BPT diagram (Medling et al. 2015), we do not see evidence for mergers in the NIRCam imaging for any of our galaxies, although we note that merger signatures may disappear on short timescales, so features such as tidal tails might not be visible. It is therefore likely that the high emission line ratios for these galaxies are due to AGN activity.

Several studies have also found evidence for AGN activity using line ratio diagnostics in quenching or quenched galaxies at cosmic noon (e.g. Belli et al. 2024; D'Eugenio et al. 2024; Bugiani et al. 2024) and in the local Universe (e.g. Yesuf et al. 2014; Pawlik et al. 2018). Fast outflows (∼ 1000 km s⁻¹) at $z > 1$ seen in quenched galaxies have been interpreted as being driven by AGN activity, as these galaxies have low current star formation rates and the outflows are detected

long (> 0.6 Gyr) after the peak in star formation (Taylor et al. 2024). In a sample of quiescent galaxies at cosmic noon from the Blue Jay survey, Bugiani et al. (2024) found that 60% of the galaxies reliably classified from line ratios show signs of hosting an AGN. This is consistent with the 50% of galaxies in our sample with reliable classifications showing evidence of AGN activity. None of the galaxies in our sample are detected in the X-ray in *Chandra* by the X-UDS survey (PI: G. Hasinger; Kocevski et al. 2018), and only one galaxy (EXCELS – 94982) is detected in the radio (Patil et al. in prep). Bugiani et al. (2024) similarly found that none of the quiescent galaxies in their sample are detected in the X-rays or radio. Additionally, none of the 7 sources with MIRI F1800W coverage are detected (Hewitt, private communication) and none of our 24 sources are detected at 24 μm with the *Spitzer* UDS Legacy Program (SpUDS, PI:Dunlop where the data is available in IRSA (SpUDS team 2020)), implying a lack of AGN-heated dust.

In the local Universe, Lanz et al. (2022) find that half of their sample of 12 PSBs show evidence of AGN activity with low X-ray luminosities, and suggest that AGN may be 'along for the ride', having been fueled by the same processes that caused the starburst and/or quenching episode. At cosmic noon ($0.5 < z < 3$), there is no evidence for enhanced X-ray AGN activity in PSBs, with the observed weak AGN activity consistent with the low star formation rates (Almaini et al. 2025). Patil et al. (in prep) similarly find low detection rates of PSBs at cosmic noon in the radio, and a stacking analysis reveals very weak AGN activity or low-level star formation in the most massive post-starburst galaxies. This is consistent with the lack of radio and X-ray detections in quenching galaxies at cosmic noon, despite the high AGN fractions inferred from line ratios. It is also possible that the galaxies in our sample are classified as AGN due to their higher mass, which makes it easier to detect weak AGN. Indeed, of the galaxies in our sample with both line ratios available, the more massive galaxies with higher star formation rates tend to be classified as AGN based on line ratio diagnostics. Careful consideration of the sample selection, particularly the mass limits, is essential, as biases make it difficult to draw definitive conclusions.

Placing constraints on the gas reservoirs of quenching galaxies is important for constraining the physical mechanism(s) involved in quenching. The discovery of molecular gas reservoirs in post-starburst galaxies challenges the notion that quenching occurs solely due to gas starvation (e.g. Rowlands et al. 2015; Bezanson et al. 2022). The recent detection of molecular gas in a quies-

cent $z \sim 3$ galaxy (Umehata et al. 2025) further suggests that quenching galaxies at cosmic noon may be quenching star formation due to additional processes beyond gas depletion. However, even if reservoirs of cold gas remain in our sample, occasional bursts of AGN activity may suppress star formation via ejective or maintenance mode feedback. Using cosmological simulations, Kimmig et al. (2025) find that while AGN feedback is important in quenching galaxies, a rapid starburst followed by gas removal from AGN is the dominant quenching mechanism down to $z \sim 2$. This scenario seems plausible for the galaxies in our sample with strong starbursts followed by fast quenching times.

The lack of X-ray and radio detections in our sample may be due to short AGN duty cycles, as the evidence for AGN activity based on line ratio diagnostics may reflect past AGN episodes (French et al. 2023). It is also possible that our sources are obscured or that the AGN are very weak, though still able to suppress star formation by disturbing the gas reservoir (Smercina et al. 2022; Luo et al. 2022). AGN may play a crucial role in maintaining quiescence (e.g. Kimmig et al. 2025), but AGN feedback does not seem to be the primary quenching driver, as our observations suggest that the driver is a combination of gas exhaustion and stellar feedback from a recent starburst.

5. CONCLUSIONS

We present a sample of 24 quenching and quenched massive ($\log M_*/M_\odot > 10$) galaxies at $1 < z < 3$ with medium-resolution NIRSpec spectroscopy from the EX-CELS survey. We fit both the observed photometry and spectroscopy using BAGPIPES to infer their star formation histories and emission line properties. Our conclusions are summarized as follows:

1. We confirm that the PCA photometric (super-color) selection of quiescent and post-starburst galaxies, first established by Wild et al. (2014), is robust up to redshifts of $z \sim 3$ using EXCELS spectroscopy. Within the post-starburst region of the super-color diagram, we find a tentative trend with the super-color values and the burst age, with younger post-starburst galaxies having higher values of super-color 1 and super-color 2.

2. We find that the median post-starburst visibility time is 612 Myr, ranging from 50 Myr to 894 Myr as shown in Figure 7. Six out of nine of the quiescent galaxies in our sample are predicted to have entered the PSB region during their evolution, with the others quenching more slowly. PSBs are an important pathway for the growth of the quiescent galaxy population. Based on our predicted visibility times, PSBs potentially account for $\sim 73\%$ of the growth of quiescent galaxies at the highest stellar masses ($\log M_*/M_\odot > 10.7$).

3. We see a variety of SFHs, with the majority of the sample undergoing rapid quenching following a burst of star formation. The inferred maximum star formation rates of these galaxies (see Figure 9) are consistent with many of them being the descendants of SMGs. We find that the number densities of galaxies in our sample that went through an SMG phase between $1.4 < z < 4.6$ are consistent with the number density of SMGs, and predict that SMGs are visible for ~ 70 Myr based on our SFHs.

4. In Figure 10, we show that the quenching timescales in our sample span 0.06-1.75 Gyr. This wide range of quenching timescales suggests different quenching pathways may be at work.

5. We find that 4 out of 8 galaxies with robust line detections in our sample show evidence for AGN activity based on rest-frame optical line diagnostics (see Figure 8), despite none of these sources having X-ray or radio detections. This is consistent with other works at the same redshift (e.g. Bugiani et al. 2024).

There is likely a range of quenching mechanisms at $z \sim 2$, resulting in the build-up of the quiescent galaxy population. We suggest that many of these galaxies may quench rapidly following a starburst due to stellar feedback and gas exhaustion, with AGN possibly playing a role in maintaining quiescence. Future work using larger samples of $JWST$/NIRSpec observations will enable more robust tests of how post-starburst galaxy properties vary with burst age, providing deeper insights into the mechanisms driving quenching.

Facilities: JWST(NIRSpec), JWST(NIRCam), HST(ACS), JWST(MIRI), VLT

Software: Astropy (Astropy Collaboration et al. 2013, 2018, 2022), Bagpipes (Carnall et al. 2018, 2019), pPXF (Cappellari 2023), Scipy (Virtanen et al. 2020), Numpy (Harris et al. 2020), Matplotlib (Hunter 2007), spectres (Carnall 2017)

APPENDIX

A. SPECTRA FOR SAMPLE OF GALAXIES

In Figure 11, we show the rest-frame spectra for our sample of galaxies.

REFERENCES

Almaini, O., Wild, V., Maltby, D. T., et al. 2017, MNRAS, 472, 1401, doi: 10.1093/mnras/stx1957

Almaini, O., Wild, V., Maltby, D., et al. 2025, MNRAS, 539, 3568, doi: 10.1093/mnras/staf659
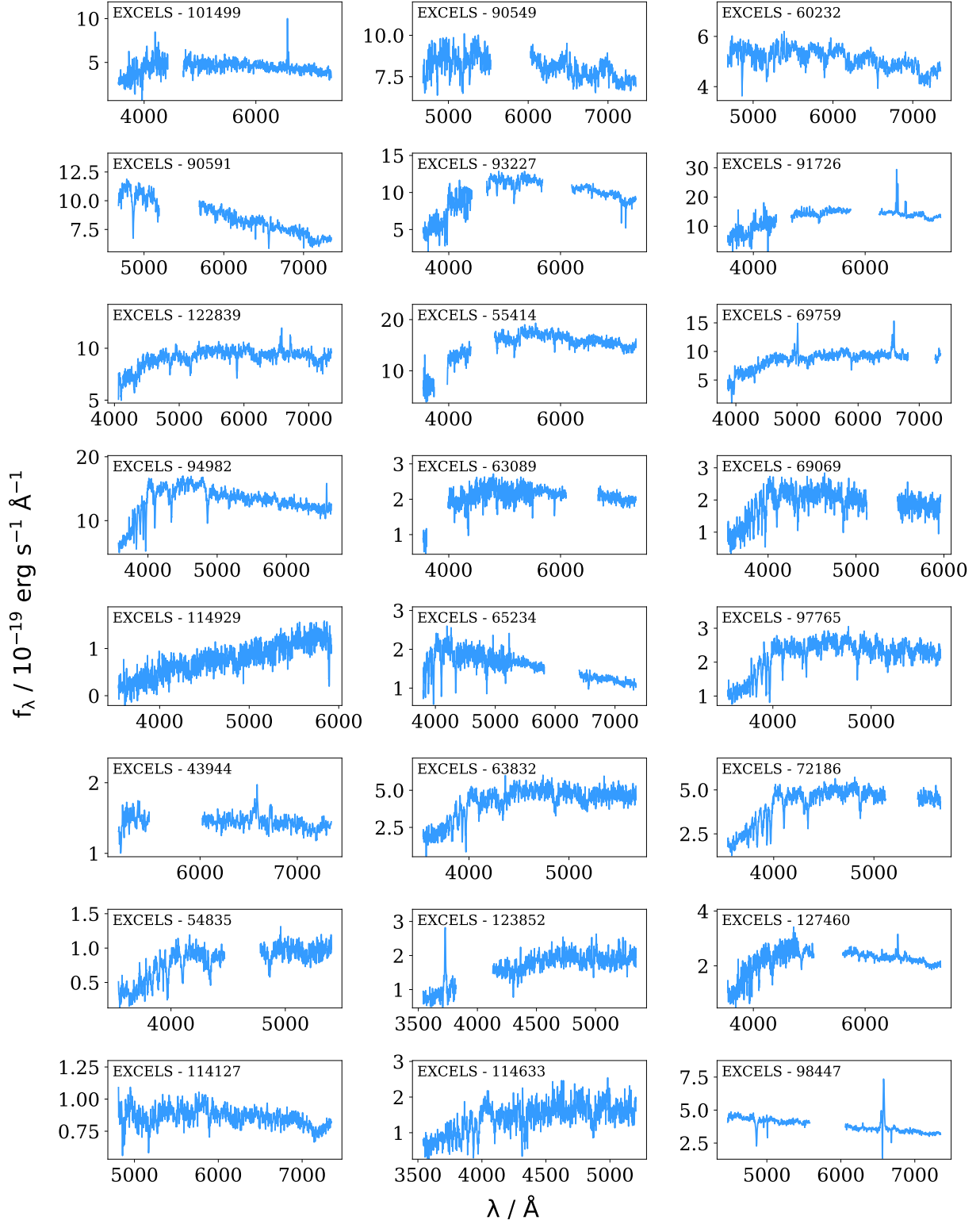
Figure 11. Rest-frame spectra for our sample of galaxies in the 3540 to 7350Å range, sorted by redshift.

Arnouts, S., Walcher, C. J., Le Fèvre, O., et al. 2007, A&A, 476, 137, doi: 10.1051/0004-6361:20077632

Astropy Collaboration, Robitaille, T. P., Tollerud, E. J., et al. 2013, A&A, 558, A33, doi: 10.1051/0004-6361/201322068

Astropy Collaboration, Price-Whelan, A. M., Sipőcz, B. M., et al. 2018, AJ, 156, 123, doi: 10.3847/1538-3881/aabc4f

Astropy Collaboration, Price-Whelan, A. M., Lim, P. L., et al. 2022, ApJ, 935, 167, doi: 10.3847/1538-4357/ac7c74

Baldwin, J. A., Phillips, M. M., & Terlevich, R. 1981, PASP, 93, 5, doi: 10.1086/130766

Bell, E. F., Wolf, C., Meisenheimer, K., et al. 2004, ApJ, 608, 752, doi: 10.1086/420778

Belli, S., Newman, A. B., & Ellis, R. S. 2019, ApJ, 874, 17, doi: 10.3847/1538-4357/ab07af

Belli, S., Park, M., Davies, R. L., et al. 2024, Nature, 630, 54, doi: 10.1038/s41586-024-07412-1

Bertin, E., & Arnouts, S. 1996, A&AS, 117, 393, doi: 10.1051/aas:1996164

Bezanson, R., Spilker, J. S., Suess, K. A., et al. 2022, ApJ, 925, 153, doi: 10.3847/1538-4357/ac3dfa

Brinchmann, J., Charlot, S., White, S. D. M., et al. 2004, MNRAS, 351, 1151, doi: 10.1111/j.1365-2966.2004.07881.x

Bruzual, G., & Charlot, S. 2003, MNRAS, 344, 1000, doi: 10.1046/j.1365-8711.2003.06897.x

Buchner, J., Georgakakis, A., Nandra, K., et al. 2014, A&A, 564, A125, doi: 10.1051/0004-6361/201322971

Bugiani, L., Belli, S., Park, M., et al. 2024, arXiv e-prints, arXiv:2406.08547, doi: 10.48550/arXiv.2406.08547

Cappellari, M. 2017, MNRAS, 466, 798, doi: 10.1093/mnras/stw3020

—. 2023, MNRAS, 526, 3273, doi: 10.1093/mnras/stad2597

Cappellari, M., & Emsellem, E. 2004, PASP, 116, 138, doi: 10.1086/381875

Carnall, A. C. 2017, arXiv e-prints, arXiv:1705.05165, doi: 10.48550/arXiv.1705.05165

Carnall, A. C., McLure, R. J., Dunlop, J. S., & Davé, R. 2018, MNRAS, 480, 4379, doi: 10.1093/mnras/sty2169

Carnall, A. C., McLure, R. J., Dunlop, J. S., et al. 2019, MNRAS, 490, 417, doi: 10.1093/mnras/stz2544

—. 2023, Nature, 619, 716, doi: 10.1038/s41586-023-06158-6

Carnall, A. C., Cullen, F., McLure, R. J., et al. 2024, MNRAS, 534, 325, doi: 10.1093/mnras/stae2092

Chen, Y.-M., Shi, Y., Wild, V., et al. 2019, MNRAS, 489, 5709, doi: 10.1093/mnras/stz2494

Cid Fernandes, R., Stasińska, G., Mateus, A., & Vale Asari, N. 2011, MNRAS, 413, 1687, doi: 10.1111/j.1365-2966.2011.18244.x

Cid Fernandes, R., Stasińska, G., Schlickmann, M. S., et al. 2010, MNRAS, 403, 1036, doi: 10.1111/j.1365-2966.2009.16185.x

Conroy, C., Graves, G. J., & van Dokkum, P. G. 2014, ApJ, 780, 33, doi: 10.1088/0004-637X/780/1/33

Conroy, C., & Gunn, J. E. 2010, ApJ, 712, 833, doi: 10.1088/0004-637X/712/2/833

Conroy, C., Gunn, J. E., & White, M. 2009, ApJ, 699, 486, doi: 10.1088/0004-637X/699/1/486

Conroy, C., & van Dokkum, P. G. 2012, ApJ, 760, 71, doi: 10.1088/0004-637X/760/1/71

Davies, R. L., Belli, S., Park, M., et al. 2024, MNRAS, 528, 4976, doi: 10.1093/mnras/stae327

D'Eugenio, C., Daddi, E., Gobat, R., et al. 2020, ApJL, 892, L2, doi: 10.3847/2041-8213/ab7a96

D'Eugenio, F., Pérez-González, P. G., Maiolino, R., et al. 2024, Nature Astronomy, 8, 1443, doi: 10.1038/s41550-024-02345-1

Dunlop, J. S., Abraham, R. G., Ashby, M. L. N., et al. 2021, PRIMER: Public Release IMaging for Extragalactic Research, JWST Proposal. Cycle 1, ID. #1837

Estrada-Carpenter, V., Papovich, C., Momcheva, I., et al. 2020, ApJ, 898, 171, doi: 10.3847/1538-4357/aba004

Falcón-Barroso, J., Sánchez-Blázquez, P., Vazdekis, A., et al. 2011, A&A, 532, A95, doi: 10.1051/0004-6361/201116842

Feroz, F., Hobson, M. P., Cameron, E., & Pettitt, A. N. 2019, The Open Journal of Astrophysics, 2, 10, doi: 10.21105/astro.1306.2144

Fontana, A., Pozzetti, L., Donnarumma, I., et al. 2004, A&A, 424, 23, doi: 10.1051/0004-6361:20035626

French, K. D. 2021, PASP, 133, 072001, doi: 10.1088/1538-3873/ac0a59

French, K. D., Earl, N., Novack, A. B., et al. 2023, ApJ, 950, 153, doi: 10.3847/1538-4357/acd249

Garilli, B., McLure, R., Pentericci, L., et al. 2021, A&A, 647, A150, doi: 10.1051/0004-6361/202040059

Gillman, S., Smail, I., Gullberg, B., et al. 2024, A&A, 691, A299, doi: 10.1051/0004-6361/202451006

Grogin, N. A., Kocevski, D. D., Faber, S. M., et al. 2011, ApJS, 197, 35, doi: 10.1088/0067-0049/197/2/35

Harris, C. R., Millman, K. J., van der Walt, S. J., et al. 2020, Nature, 585, 357, doi: 10.1038/s41586-020-2649-2

Hayward, C. C., Kereš, D., Jonsson, P., et al. 2011, ApJ, 743, 159, doi: 10.1088/0004-637X/743/2/159

Hopkins, P. F., Cox, T. J., Kereš, D., & Hernquist, L. 2008a, ApJS, 175, 390, doi: 10.1086/524363

Hopkins, P. F., Hernquist, L., Cox, T. J., Dutta, S. N., & Rothberg, B. 2008b, ApJ, 679, 156, doi: 10.1086/587544

Horne, K. 1986, PASP, 98, 609, doi: 10.1086/131801

Hunter, J. D. 2007, Computing in Science & Engineering, 9, 90, doi: 10.1109/MCSE.2007.55

Ilbert, O., McCracken, H. J., Le Fèvre, O., et al. 2013, A&A, 556, A55, doi: 10.1051/0004-6361/201321100

Ji, Z., Williams, C. C., Suess, K. A., et al. 2024, arXiv e-prints, arXiv:2401.00934, doi: 10.48550/arXiv.2401.00934

Kauffmann, G., Heckman, T. M., White, S. D. M., et al. 2003a, MNRAS, 341, 33, doi: 10.1046/j.1365-8711.2003.06291.x

Kauffmann, G., Heckman, T. M., Tremonti, C., et al. 2003b, MNRAS, 346, 1055, doi: 10.1111/j.1365-2966.2003.07154.x

Kaviraj, S., Kirkby, L. A., Silk, J., & Sarzi, M. 2007, MNRAS, 382, 960, doi: 10.1111/j.1365-2966.2007.12475.x

Kaviraj, S., Schawinski, K., Silk, J., & Shabala, S. S. 2011, MNRAS, 415, 3798, doi: 10.1111/j.1365-2966.2011.19002.x

Kewley, L. J., Heisler, C. A., Dopita, M. A., & Lumsden, S. 2001, ApJS, 132, 37, doi: 10.1086/318944

Kewley, L. J., Maier, C., Yabe, K., et al. 2013, ApJL, 774, L10, doi: 10.1088/2041-8205/774/1/L10

Kewley, L. J., Nicholls, D. C., & Sutherland, R. S. 2019, ARA&A, 57, 511, doi: 10.1146/annurev-astro-081817-051832

Khalatyan, A., Cattaneo, A., Schramm, M., et al. 2008, MNRAS, 387, 13, doi: 10.1111/j.1365-2966.2008.13093.x

Kimmig, L. C., Remus, R.-S., Seidel, B., et al. 2025, ApJ, 979, 15, doi: 10.3847/1538-4357/ad9472

Kocevski, D. D., Hasinger, G., Brightman, M., et al. 2018, ApJS, 236, 48, doi: 10.3847/1538-4365/aab9b4

Koekemoer, A. M., Faber, S. M., Ferguson, H. C., et al. 2011, ApJS, 197, 36, doi: 10.1088/0067-0049/197/2/36

Kroupa, P. 2001, MNRAS, 322, 231, doi: 10.1046/j.1365-8711.2001.04022.x

Lagos, C. d. P., Valentino, F., Wright, R. J., et al. 2025, MNRAS, 536, 2324, doi: 10.1093/mnras/stae2626

Lang, P., Schinnerer, E., Smail, I., et al. 2019, ApJ, 879, 54, doi: 10.3847/1538-4357/ab1f77

Lanz, L., Stepanoff, S., Hickox, R. C., et al. 2022, ApJ, 935, 29, doi: 10.3847/1538-4357/ac7d56

Leung, H.-H., Wild, V., Papathomas, M., et al. 2024, MNRAS, 528, 4029, doi: 10.1093/mnras/stae225

Luo, Y., Rowlands, K., Alatalo, K., et al. 2022, ApJ, 938, 63, doi: 10.3847/1538-4357/ac8b7d

Maltby, D. T., Almaini, O., Wild, V., et al. 2018, MNRAS, 480, 381, doi: 10.1093/mnras/sty1794

—. 2016, MNRAS, 459, L114, doi: 10.1093/mnrasl/slw057

McLeod, D. J., McLure, R. J., Dunlop, J. S., et al. 2021, MNRAS, 503, 4413, doi: 10.1093/mnras/stab731

McLure, R. J., Pentericci, L., Cimatti, A., et al. 2018, MNRAS, 479, 25, doi: 10.1093/mnras/sty1213

Medling, A. M., U, V., Rich, J. A., et al. 2015, MNRAS, 448, 2301, doi: 10.1093/mnras/stv081

Mihos, J. C., & Hernquist, L. 1996, ApJ, 464, 641, doi: 10.1086/177353

Moutard, T., Arnouts, S., Ilbert, O., et al. 2016, A&A, 590, A103, doi: 10.1051/0004-6361/201527294

Muzzin, A., Marchesini, D., Stefanon, M., et al. 2013, ApJ, 777, 18, doi: 10.1088/0004-637X/777/1/18

Nanayakkara, T., Glazebrook, K., Jacobs, C., et al. 2024, Scientific Reports, 14, 3724, doi: 10.1038/s41598-024-52585-4

Pacifici, C., Kassin, S. A., Weiner, B. J., et al. 2016, ApJ, 832, 79, doi: 10.3847/0004-637X/832/1/79

Park, M., Belli, S., Conroy, C., et al. 2023, ApJ, 953, 119, doi: 10.3847/1538-4357/acd54a

—. 2024, ApJ, 976, 72, doi: 10.3847/1538-4357/ad7e15

Pawlik, M. M., Taj Aldeen, L., Wild, V., et al. 2018, MNRAS, 477, 1708, doi: 10.1093/mnras/sty589

Peng, Y., Maiolino, R., & Cochrane, R. 2015, Nature, 521, 192, doi: 10.1038/nature14439

Pentericci, L., McLure, R. J., Garilli, B., et al. 2018, A&A, 616, A174, doi: 10.1051/0004-6361/201833047

Petersson, J., Renaud, F., Agertz, O., Dekel, A., & Duc, P.-A. 2023, MNRAS, 518, 3261, doi: 10.1093/mnras/stac3136

Rowlands, K., Wild, V., Nesvadba, N., et al. 2015, MNRAS, 448, 258, doi: 10.1093/mnras/stu2714

Rowlands, K., Wild, V., Bourne, N., et al. 2018, MNRAS, 473, 1168, doi: 10.1093/mnras/stx1903

Sánchez-Blázquez, P., Peletier, R. F., Jiménez-Vicente, J., et al. 2006, MNRAS, 371, 703, doi: 10.1111/j.1365-2966.2006.10699.x

Schawinski, K., Urry, C. M., Simmons, B. D., et al. 2014, MNRAS, 440, 889, doi: 10.1093/mnras/stu327

Setton, D. J., Khullar, G., Miller, T. B., et al. 2024, ApJ, 974, 145, doi: 10.3847/1538-4357/ad6a18

Simpson, J. M., Smail, I., Swinbank, A. M., et al. 2015, ApJ, 799, 81, doi: 10.1088/0004-637X/799/1/81

Slob, M., Kriek, M., Beverage, A. G., et al. 2024, ApJ, 973, 131, doi: 10.3847/1538-4357/ad65ff

Smercina, A., Smith, J.-D. T., French, K. D., et al. 2022, ApJ, 929, 154, doi: 10.3847/1538-4357/ac5d5f

Speagle, J. S., Steinhardt, C. L., Capak, P. L., & Silverman, J. D. 2014, ApJS, 214, 15, doi: 10.1088/0067-0049/214/2/15

Springel, V., Di Matteo, T., & Hernquist, L. 2005, ApJL, 620, L79, doi: 10.1086/428772

SpUDS team. 2020, Spitzer Public Legacy Survey of the
UKIDSS Ultra Deep Survey (SpUDS), IPAC,
doi: 10.26131/IRSA403

Swinbank, A. M., Simpson, J. M., Smail, I., et al. 2014,
MNRAS, 438, 1267, doi: 10.1093/mnras/stt2273

Tacchella, S., Conroy, C., Faber, S. M., et al. 2022, ApJ,
926, 134, doi: 10.3847/1538-4357/ac449b

Taylor, E., Almaini, O., Merrifield, M., et al. 2023,
MNRAS, 522, 2297, doi: 10.1093/mnras/stad1098

Taylor, E., Maltby, D., Almaini, O., et al. 2024, MNRAS,
535, 1684, doi: 10.1093/mnras/stae2463

Tremonti, C. A., Heckman, T. M., Kauffmann, G., et al.
2004, ApJ, 613, 898, doi: 10.1086/423264

Umehata, H., Kubo, M., & Nakanishi, K. 2025, arXiv
e-prints, arXiv:2502.06538,
doi: 10.48550/arXiv.2502.06538

Valentino, F., Heintz, K. E., Brammer, G., et al. 2025,
arXiv e-prints, arXiv:2503.01990,
doi: 10.48550/arXiv.2503.01990

Virtanen, P., Gommers, R., Oliphant, T. E., et al. 2020,
Nature Methods, 17, 261, doi: 10.1038/s41592-019-0686-2

Weaver, J. R., Davidzon, I., Toft, S., et al. 2023, A&A, 677,
A184, doi: 10.1051/0004-6361/202245581

Wellons, S., Torrey, P., Ma, C.-P., et al. 2015, MNRAS,
449, 361, doi: 10.1093/mnras/stv303

Whitaker, K. E., Kriek, M., van Dokkum, P. G., et al. 2012,
ApJ, 745, 179, doi: 10.1088/0004-637X/745/2/179

Wild, V., Almaini, O., Dunlop, J., et al. 2016, MNRAS,
463, 832, doi: 10.1093/mnras/stw1996

Wild, V., Kauffmann, G., Heckman, T., et al. 2007,
MNRAS, 381, 543, doi: 10.1111/j.1365-2966.2007.12256.x

Wild, V., Almaini, O., Cirasuolo, M., et al. 2014, MNRAS,
440, 1880, doi: 10.1093/mnras/stu212

Wild, V., Taj Aldeen, L., Carnall, A., et al. 2020, MNRAS,
494, 529, doi: 10.1093/mnras/staa674

Wilkinson, A., Almaini, O., Wild, V., et al. 2021, MNRAS,
504, 4533, doi: 10.1093/mnras/stab965

Williams, R. J., Quadri, R. F., Franx, M., van Dokkum, P.,
& Labbé, I. 2009, ApJ, 691, 1879,
doi: 10.1088/0004-637X/691/2/1879

Worthey, G., & Ottaviani, D. L. 1997, ApJS, 111, 377,
doi: 10.1086/313021

Wright, R. J., Lagos, C. d. P., Davies, L. J. M., et al. 2019,
MNRAS, 487, 3740, doi: 10.1093/mnras/stz1410

Wu, P.-F. 2025, ApJ, 978, 131,
doi: 10.3847/1538-4357/ad98ef

Wu, P.-F., van der Wel, A., Bezanson, R., et al. 2018, ApJ,
868, 37, doi: 10.3847/1538-4357/aae822

Yesuf, H. M., Faber, S. M., Trump, J. R., et al. 2014, ApJ,
792, 84, doi: 10.1088/0004-637X/792/2/84

Zheng, Y., Wild, V., Lahén, N., et al. 2020, MNRAS, 498,
1259, doi: 10.1093/mnras/staa2358

Zolotov, A., Dekel, A., Mandelker, N., et al. 2015, MNRAS,
450, 2327, doi: 10.1093/mnras/stv740